Depth dependence of permeability in the Oregon Cascades inferred from hydrogeologic, thermal, seismic, and magmatic modeling constraints

M. O. Saar[1]
Department of Geological Sciences, University of Michigan, Ann Arbor, Michigan, USA

M. Manga[1]
Department of Earth and Planetary Science, University of California, Berkeley, California, USA

Received 16 October 2003; revised 27 January 2004; accepted 20 February 2004; published 20 April 2004.

[1] We investigate the decrease in permeability, k, with depth, z, in the Oregon Cascades employing four different methods. Each method provides insight into the average permeability applicable to a different depth scale. Spring discharge models are used to infer shallow ($z < 0.1$ km) horizontal permeabilities. Coupled heat and groundwater flow simulations provide horizontal and vertical k for $z < 1$ km. Statistical investigations of the occurrences of earthquakes that are probably triggered by seasonal groundwater recharge yield vertical k for $z < 5$ km. Finally, considerations of magma intrusion rates and water devolatilization provide estimates of vertical k for $z < 15$ km. For depths >0.8 km, our results agree with the power law relationship, $k = 10^{-14}$ m^2 $(z/1\text{ km})^{-3.2}$, suggested by *Manning and Ingebritsen* [1999] for continental crust in general. However, for shallower depths (typically $z \leq 0.8$ km and up to $z \leq 2$) we propose an exponential relationship, $k = 5 \times 10^{-13}$ m^2 exp $(-z/0.25\text{ km})$, that both fits data better (at least for the Cascades and seemingly for continental crust in general) and allows for a finite near-surface permeability and no singularity at zero depth. In addition, the suggested functions yield a smooth transition at $z = 0.8$ km, where their permeabilities and their gradients are similar. Permeabilities inferred from the hydroseismicity model at Mount Hood are about one order of magnitude larger than expected from the above power law. However, higher permeabilities in this region may be consistent with advective heat transfer along active faults, causing observed hot springs. Our simulations suggest groundwater recharge rates of $0.5 \leq u_R \leq 1$ m/yr and a mean background heat flow of $H_b \approx 0.080$–0.134 W/m^2 for the investigated region. *INDEX TERMS:* 1829 Hydrology: Groundwater hydrology; 1878 Hydrology: Water/energy interactions; 3210 Mathematical Geophysics: Modeling; 5114 Physical Properties of Rocks: Permeability and porosity; 8424 Volcanology: Hydrothermal systems (8135); *KEYWORDS:* permeability, scale, heterogeneity

Citation: Saar, M. O., and M. Manga (2004), Depth dependence of permeability in the Oregon Cascades inferred from hydrogeologic, thermal, seismic, and magmatic modeling constraints, *J. Geophys. Res.*, *109*, B04204, doi:10.1029/2003JB002855.

1. Introduction

[2] Permeability, **k**, describes a material's ability to transmit fluids. It is thus a critical material property, relevant to numerous geological processes that depend on mass and/or energy transfer as described for example by *Ingebritsen and Sanford* [1998]. Examples include transfer of water, steam, hydrocarbons, pore fluid pressure, and heat. Permeability is a second rank tensor that can be highly anisotropic and heterogeneous, varying over more than 15 orders of magnitude in geological materials [e.g., *Freeze and Cherry*, 1979]. Because fluid driving forces and viscosities vary much less, permeability is the most important parameter in geological porous media flow, largely determining fluid fluxes. Measuring the permeability of rock cores in laboratory settings [e.g., *Brace*, 1980, 1984; *Saar and Manga*, 1999] is done routinely. However, such rock core permeabilities may not reflect field-scale values [e.g., *Clauser*, 1992; *Sánchez-Vila et al.*, 1996; *Hyun et al.*, 2002] where larger representative elementary volumes [*Bear*, 1988] may have to be considered that include large-scale fractures or layers. At intermediate field scales, from tens to hundreds of meters, it is frequently possible to conduct pumping or slug tests to determine **k**. However, to investigate permeability distributions at tens to thousands of meters, it is necessary to employ analytical or numerical models that are constrained by (sometimes indirect) observations [*Manning and Ingebritsen*, 1999].

[1] Also at Earth Science Division, Lawrence Berkeley National Laboratory, Berkeley, California, USA.

0148-0227/04/2003JB002855$09.00

[3] Because **k** affects mass and energy transfer, it is in principle possible to use various observations as constraints or boundary conditions in models to estimate **k**, provided that the observations depend on, or determine, mass and/or energy transport. Possible constraints and boundary conditions include classical hydrogeologic parameters such as surface water infiltration rates, hydraulic head distribution, spring discharge, and no flow boundaries. Other observations may include subsurface temperature distribution, heat flow, rock metamorphism, mineral precipitation, chemical or biological fluid-rock interactions, pore fluid pressure variations and related seismicity, magma intrusions providing heat and volatiles, and concentrations of fluids and isotopes.

[4] Hydrogeologic models are typically underconstrained, particularly at large scales. Therefore utilizing multiple constraints is desirable. Despite the inherent difficulties of constraining fluid flow models, it is often the regional, large-scale permeability distribution that has important implications for geological processes. These processes and applications include regional groundwater flow patterns, long-term water management, coupled heat and fluid transfer, geothermal energy exploration, carbon sequestration, subsurface waste fluid injection, and mineral, oil, and gas exploration.

[5] The Cascades arc is a volcanic range located along an active, convergent plate boundary. In this paper we determine permeability, **k**, as a function of depth, z, in the upper crust of the Oregon Cascades (Figure 1). We also find evidence supporting a similar $k(z)$ profile in continental crust in general.

[6] We use four different modeling approaches to estimate one-dimensional permeability (vertical or horizontal) at four different depth scales: (1) A spring discharge model provides insight into (mostly) horizontal permeability values at depths of $z < 0.1$ km; (2) analytic and numerical models of coupled heat and groundwater transfer provide horizontal and vertical k at depth scales of about $z < 1$ km; (3) studies of seismicity induced by groundwater recharge allow for estimates of vertical k at approximately $z < 5$ km; finally, (4) magma intrusion and degassing models provide insight into permeabilities at the largest depth scale considered here of about $z <$ 15 km. Methods from scale 1 as well as methods and results from scale 3 are based on previous publications [*Manga*, 1997, 1999; *Saar and Manga*, 2003] and are summarized, applied, and interpreted here to fit the objective of this paper. Methods and results from scales 2 and 4 are original to this publication and are thus described in more detail.

[7] We compare our results for permeability as a function of depth for the upper crust of the Oregon Cascades with the permeability-depth curve compiled by *Manning and Ingebritsen* [1999] for continental crust in general and show that there is good agreement for depths larger than about 1 km. For depths smaller than approximately 1 km, we propose an exponential permeability curve that both fits data better and allows for a finite near-surface permeability. In addition, from our study of coupled heat and groundwater transfer (scale 2) we infer regional geothermal background heat flow and groundwater recharge rates.

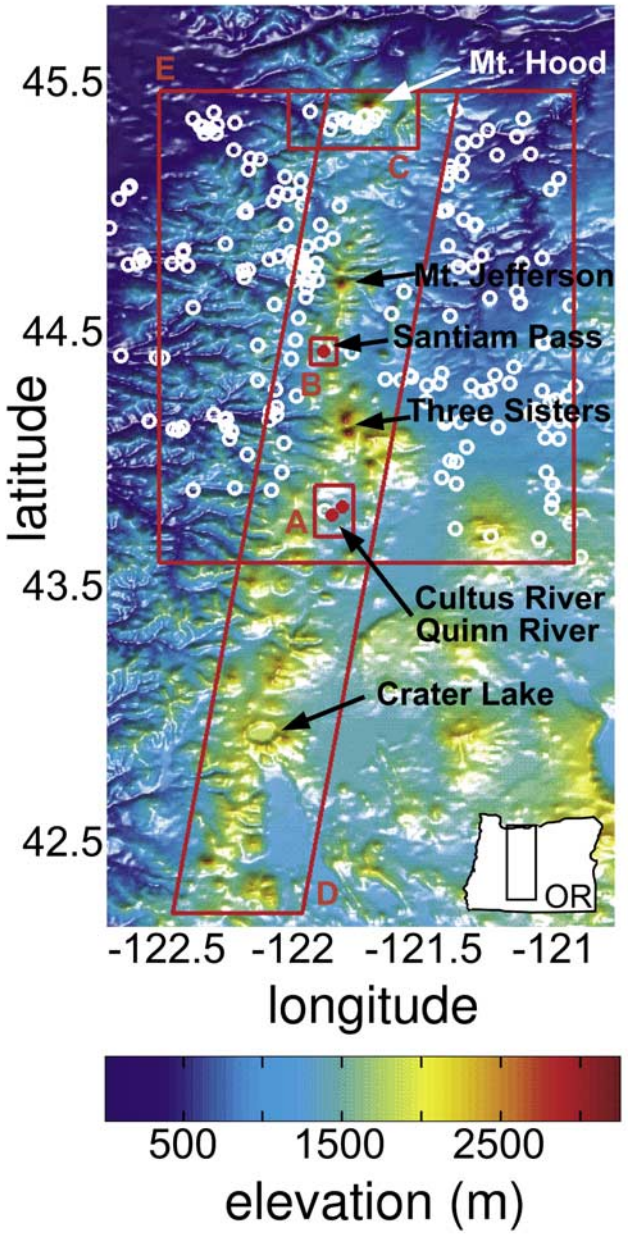

Figure 1. Shaded relief map of the study region in Oregon, USA. Red boxes indicate particular study regions used for the four methods and scales described in section 2: spring discharge model (A), coupled heat and groundwater flow model in a one-dimensional (1-D) recharge area (B), radial coupled heat and groundwater flow model (C), magma intrusion model (D), and region for heat flow interpolation based on 209 geotherm profiles (E) (white circles).

2. Four Depth Scales of k

[8] We investigate permeability, **k**, at four different depth scales which are considered representative elementary volumes of four different sizes that are in themselves homogeneous but possibly anisotropic. In this section we present methods and results starting at the smallest (shallowest) and proceeding toward the largest (deepest) scale. The four methods employed either provide hydraulic conductivity, **K** (in vertical, K_z, or horizontal, K_x, direction) or vertical hydraulic diffusivity, D_z. Both hydraulic conductivity and hydraulic diffusivity are converted to

Table 1. Definition of Symbols in Equations

Symbol	Units	Value	Definition
α	m^2/N	10^{-10}	vertical compressibility of bulk aquifer
β	m^2/N	4.8×10^{-10}	compressibility of water
b	m		thickness of aquifer or saturated zone
c_w	J/kg/°C	4180	specific heat of water
c_r	J/kg/°C	1000	specific heat of rock
d	m		magma intrusion or permeability depth
D	m^2/s		hydraulic diffusivity tensor
D_m	m^2/s		mixed thermal diffusivity (as scalar)
δ	m		characteristic depth scale (skin depth)
ϵ	°C		mean absolute temperature error
g	m/s^2	9.81	gravitational constant
h	m		hydraulic head
H	W/m^2		heat flow
k	m^2		permeability tensor
K	m/s		hydraulic conductivity tensor
K_{Tw}	W/m/°C	0.6	thermal conductivity of water
K_{Tr}	W/m/°C	2	thermal conductivity of rock (as scalar)
L	m		length of aquifer or volcanic arc
μ	Pa · s		dynamic viscosity
ν	m^2/s		kinematic viscosity
n		0.01	connected pore fraction
P	Pa		pore fluid pressure
Ψ	m/yr		precipitation rate
ψ	s		period
ϕ			weight fraction
Q	m^3/s		volumetric flux
ρ_w	kg/m^3	1000	density of water
ρ_r	kg/m^3	2700	density of rock
S_S	1/m		specific storage
S_Y			specific yield
T	°C		temperature
t	s		time
τ	s		diffusion timescale
u	m/s		Darcy velocity vector
v	m/s		interstitial or seepage velocity vector
W	m		width of aquifer or volcanic arc
		Subscripts	
e			elevation
M			magma
m			mixed
p			pressure
r			rock or radial distance
R			recharge
s			(near) surface or spring
T			thermal
w			water
$\mathbf{x} = (x, y)$			horizontal positions
z			vertical positions

permeability as described in section 3, so that the change in permeability as a function of depth can be discussed in section 4. Table 1 lists symbols used in this paper, their units, and their definitions.

2.1. Spring Discharge Model: $k(z < 0.1$ km)

[9] *Manga* [1997, 1999, 2001] shows that discharge at springs can be used to estimate large-scale near-surface horizontal hydraulic conductivity, K_x, and horizontal permeability, k_x. We briefly describe our approach and apply the method to discharge data from springs in the study region. We reserve interpretation for the discussion section.

2.1.1. Method

[10] Stacked lava flows form aquifers that typically show high horizontal hydraulic conductivities within the upper blocky parts of each flow [*Meinzer*, 1927; *Brace*, 1984]. The dense but jointed interior of a solidified lava flow shows predominantly vertical groundwater flow along cooling joints. *Manga* [2001] suggests that the horizontal blocky layer may be approximated as a confined aquifer of mean constant thickness, b, and high horizontal hydraulic conductivity, K_x, and the dense interior as an unconfined aquifer providing water from storage according to its specific yield, S_Y (for a sketch, see *Manga* [2001, Figure 12]). As a result, hydraulic head distribution is governed by a (one-dimensional) confined aquifer equation:

$$\frac{\partial h}{\partial t} = \frac{K_x b}{S_Y}\frac{\partial^2 h}{\partial x^2} + \frac{u_R(x,t)}{S_Y}, \tag{1}$$

where specific storage, S_S, has been substituted by S_Y/b. Here, t, x, u_R, K_x, and S_Y are time, horizontal dimension, recharge rate, horizontal hydraulic conductivity, and specific yield, respectively. The (variable) hydraulic head in the dense interior layer is denoted h. Equation (1) is equivalent to a linearized Boussinesq equation for unconfined aquifer flow, in which case b and h denote mean constant hydraulic head and small (variable) head, respectively. Equation (1) is a linear diffusion equation where the hydraulic diffusivity is given by

$$D_x = \frac{K_x b}{S_Y}. \tag{2}$$

As usual in a diffusive system, the diffusion timescale, τ, is characterized by $\tau = L^2/D_x$, where L is the aquifer length (Figure 2). Therefore equation (2) becomes

$$K_x = \frac{S_Y L^2}{b\tau}. \tag{3}$$

The aquifer thickness, b, is related to the mean residence time of water in the aquifer, $\bar{t}_r$, by

$$\bar{t}_r = \frac{AbS_Y}{\overline{Q}_s} = \frac{bS_Y}{\overline{u}_R}, \tag{4}$$

where A, $\overline{Q}_s$, and $\overline{u}_R = \overline{Q}_s/A$ are the surface area (exposed to recharge) of the unconfined aquifer, the mean spring discharge flux, and the mean groundwater recharge rate, respectively (Figure 2). Substituting equation (4) into equation (3) yields

$$K_x = \frac{S_Y^2 L^2}{\tau\, \bar{t}_r\, \overline{u}_R}. \tag{5}$$

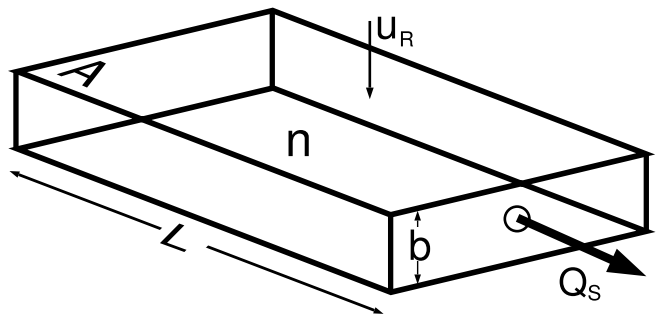

Figure 2. Spring discharge model of a simplified aquifer. Symbols are defined in the main text.

Table 2. Spring Model Input and Results for Quinn River and Cultus River

Parameter	Quinn River	Cultus River
	Input Data to Equation (5)	
$\overline{u}_R$,[a] m/yr	0.66	1.27
$\overline{t}_r$,[b] years	2.1	2.5
τ,[a] years	3.2	4.8
$S_Y \approx n$[c]	0.05–0.15	0.05–0.15
L,[d] km	10	12
	Results From Equation (5)	
$-\log K_x$, m/s	2.7–1.8	3.1–2.2

[a]From *Manga* [1997].
[b]From *James et al.* [2000].
[c]From *Ingebritsen et al.* [1992].
[d]From *Manga* [2001].

We determine horizontal hydraulic conductivity, K_x, from equation (5). Hydraulic diffusivity, D_x, and other parameters can be estimated from base flow recession curves of streams [*Hall*, 1968; *Singh and Stall*, 1971; *Tallaksen*, 1995; *Amit et al.*, 2002]. The aquifer length, L, is given by the watershed geometry and D_x is adjusted until good agreement between measured and calculated stream discharge is achieved [*Manga*, 1997, 1999]. Mean groundwater recharge, $\overline{u}_R$, can be approximated by discharge in runoff-dominated streams [*Manga*, 1996]. Specific yield, S_Y, may be approximated by connected pore fraction, n. The mean residence time, $\overline{t}_r$, for these springs is determined from radiogenic tracers [*James et al.*, 2000].

2.1.2. Results

[11] We apply equation (5) to two spring-fed streams, Cultus River and Quinn River, in the Oregon Cascades (study region A in Figure 1). The input data from both streams and results for horizontal hydraulic conductivity, K_x, are given in Table 2. For the assumed range of specific yield, $0.05 \leq S_Y \leq 0.15$, and the uncertainties implied by the number of significant digits in each input parameter (Table 2), the range of horizontal hydraulic conductivity is about

$$10^{-3} \leq K_x \leq 10^{-2} \text{ m/s}. \quad (6)$$

2.2. Coupled Heat and Groundwater Transfer Model: $k(z < 1$ km)

[12] Many studies have discussed heat and groundwater transfer in the subsurface [e.g., *Bredehoeft and Papadopulos*, 1965; *Sorey*, 1971; *Domenico and Palciauskas*, 1973; *Woodbury et al.*, 1987; *Woodbury and Smith*, 1988; *Forster and Smith*, 1989; *Ge*, 1998; *Hurwitz et al.*, 2002]. Similar to the work presented in this section, *Deming* [1993] investigates coupled heat and groundwater flow at the north slope of Alaska to estimate the local permeability on a large, regional scale. Here, we employ analytical and numerical models to simulate coupled groundwater and heat flow in a one-dimensional Cartesian and a three-dimensional cylindrical coordinate system, respectively. Owing to low temperatures present in the region of interest, we assume gravity-driven convection only and no density-driven flow. This allows us to first solve the groundwater flow equation followed by the heat advection-diffusion equation to determine the temperature field. In section 2.2.3, the temperature distribution is compared with measurements in boreholes to evaluate model input parameters.

2.2.1. Method: One-Dimensional Flow

[13] The central axis of approximately radially symmetric mountains as well as the vertical axis at the center of saddles between two such mountains may be represented by vertical one-dimensional (1-D) groundwater recharge and flow regimes (vertical lines in Figure 3). Away from the axes flow becomes 2-D or possibly 3-D. In this section, we employ analytical models of coupled groundwater and heat transfer in a 1-D recharge region.

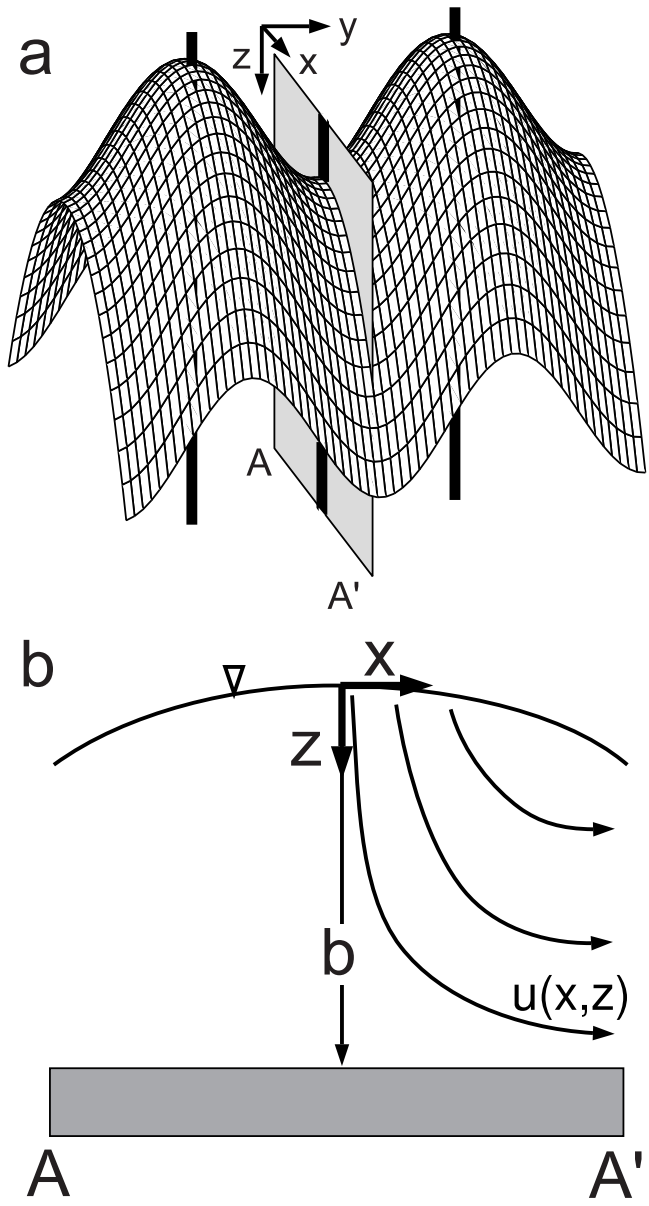

Figure 3. (a) Schematic peaks (e.g., Three Fingered Jack and Mount Washington, Oregon; see Figure 4a) and a saddle (e.g., Santiam Pass, Oregon; see Figures 1 and 4a) may represent groundwater recharge regimes with 1-D vertical groundwater flow. The saddle can also constitute a (local) groundwater discharge regime. (b) Schematic cross section A–A′ (see Figure 3a) showing a typical recharge geometry. Parameters are defined in the main text.

[14] *Phillips* [1991] derives a solution for the advection-diffusion equation, providing temperature as a function of depth, $T(z)$, in a 1-D groundwater recharge area. The solution assumes a constant mean horizontal permeability resulting in a linear decrease in vertical groundwater flow (Darcy) velocity, u_z, from a recharge (Darcy) velocity at the water table to $u_z = 0$ at the bottom of the aquifer. Here, we provide an equivalent solution for $T(z)$, equation (18), however with inverted z axis so that z is positive downward, consistent with the reference frame adopted for this paper (Figure 3). In addition, we introduce a solution to the 1-D heat advection-diffusion equation where permeability decreases exponentially with depth (equation (17)).

[15] For the remainder of this section we will refer to Darcy velocity, $\mathbf{u}$, as velocity, with the understanding that the actual interstitial (seepage) velocity is given by $\mathbf{v} = \mathbf{u}/n$, where n is the connected pore fraction. The vertical mean recharge velocity at the surface, $z = 0$, is given by $\overline{u}_R = \overline{u}_z(z = 0) = \Phi\Psi$, where Φ is the fraction of the mean yearly precipitation, Ψ, that infiltrates the ground. At the crest of the (Oregon) Cascades, typically $0.1 \leq \Phi \leq 0.5$ and $\Psi \approx 2$ m/yr so that $0.2 \leq \overline{u}_R \leq 1$ m/yr [*Ingebritsen et al.*, 1994].

[16] Following *Phillips* [1991], for an unconfined aquifer with approximately horizontal bedding, as may be expected near the symmetry axis of a saddle, the horizontal hydraulic head gradient at any depth, z, is equal to its value at the water table. Because the vertical pore fluid pressure is roughly hydrostatic, the hydraulic head is constant for any z and Darcy's law is given by

$$\mathbf{u}(\mathbf{x}, z) = -K_{\mathbf{x}}(\mathbf{x}, z)\ \nabla h(\mathbf{x}), \tag{7}$$

where $\mathbf{x} = (x, y)$ denotes both horizontal directions and $K_{\mathbf{x}}(\mathbf{x}, z)$ is the horizontal hydraulic conductivity as a function of horizontal and vertical directions. Near the symmetry axis of the saddle, the recharge velocity, u_R, and the curvature of the water table may be assumed constant. Consequently, in a 2-D cross section in the xz plane (Figure 3), considered for the remainder of this section, equation (7) may be reduced to yield the horizontal groundwater flow velocity near the vertical symmetry axis,

$$u_x(x, z) = K_x(x, z)\ \frac{x}{R}, \tag{8}$$

where $R = -(\partial^2 h/\partial x^2)^{-1}$ is the (constant) radius of curvature of the water table and thus $x/R = \nabla h(x)$. We use topography (Figure 4) to obtain $R \approx 100 \pm 20$ km.

[17] For an incompressible fluid, $\nabla \cdot \mathbf{u} = 0$. Thus for the case of constant mean horizontal hydraulic conductivity, $\overline{K}_x$, the horizontal and vertical velocities are given by

$$u_x(x) = \overline{K}_x\ \frac{x}{R} \tag{9}$$

and

$$u_z(z) = -\int \frac{\partial u_x}{\partial x} dz = \overline{K}_x\ \frac{b - z}{R}, \tag{10}$$

respectively. For equation (10) the boundary condition $u_z(z = b) = 0$ was applied to determine the integration constant. Here, b is the total vertical thickness of the saturated zone (Figure 3b). Equation (10) shows that for the case of (vertically) constant horizontal hydraulic conductivity the vertical groundwater flow velocity decreases linearly from the recharge velocity, $u_R = u_z(z = 0)$, to zero at the bottom of the aquifer at $z = b$.

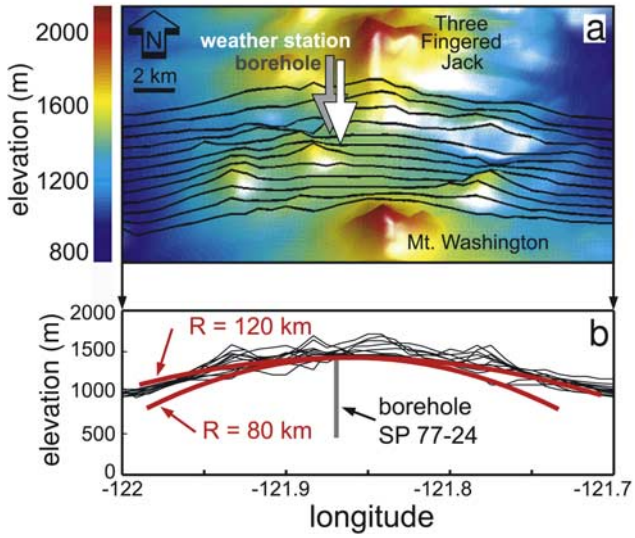

Figure 4. Radius of curvature of the ground surface at Santiam Pass, Oregon. (a) Shaded relief map between latitudes 44.25 and 44.55, color coded to elevation. Black lines indicate locations of the 12 cross sections shown in panel Figure 4b. The geothermal borehole location is indicated by the gray arrow. Weather station 357559 (U.S. Department of Commerce, National Oceanic and Atmospheric Administration (NOAA)) is indicated by the white arrow. (b) East-west elevation profiles (thin black lines) used to estimate the minimum ($R = 80$ km) and maximum ($R = 120$ km) radius of curvature (bold red curves). The borehole is shown as the gray vertical line.

[18] In contrast, for the case of (vertically) exponentially decreasing horizontal hydraulic conductivity,

$$K_x(z) = K_{sx}\ e^{-z/\delta} \tag{11}$$

as a function of depth, z, and with skin depth, δ, from a near-surface value, K_{sx}, the horizontal and vertical velocities are given by

$$u_x(x, z) = \frac{K_{sx}\ x}{R}\ e^{-z/\delta} \tag{12}$$

and

$$u_z(z) = -\int \frac{\partial u_x}{\partial x} dz = \frac{K_{sx}\delta}{R}\left(e^{-z/\delta} - 1\right) + u_R, \tag{13}$$

respectively. The boundary condition $u_z(z = 0) = u_R$ was applied in equation (13) to provide the integration constant, where the recharge velocity, u_R, is determined in Appendix A. Substituting u_R from equation (A3) in Appendix A into equation (13) results in

$$u_z(z) = \frac{K_{sx}\delta}{R}\left(e^{-z/\delta} - e^{-b/\delta}\right). \tag{14}$$

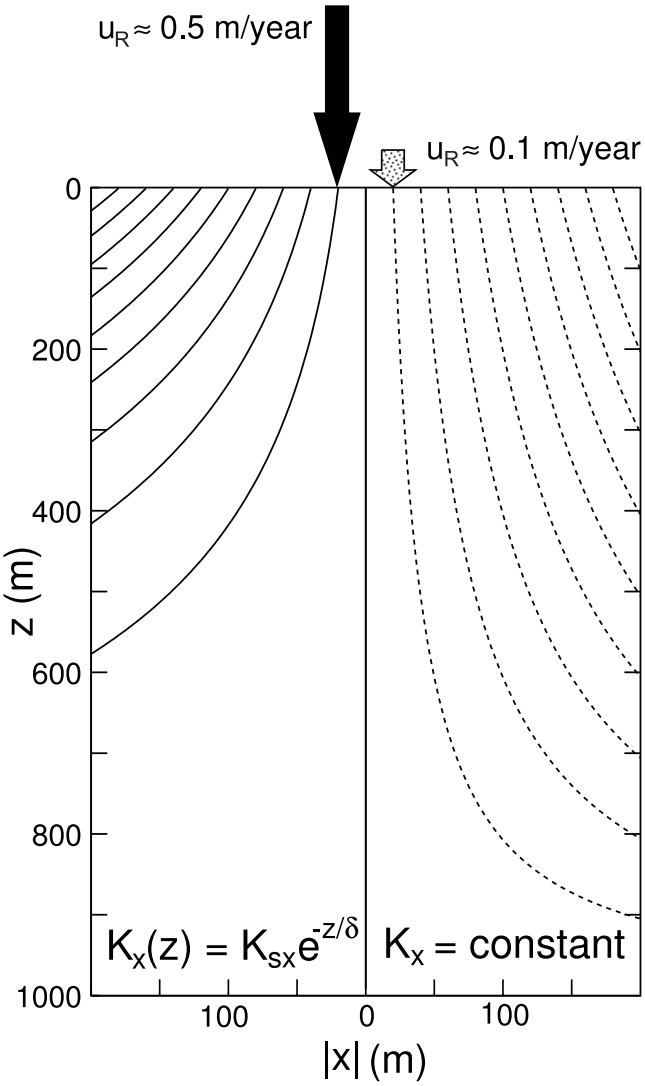

Figure 5. Groundwater flow streamlines beneath a 1-D recharge region for (vertically) exponentially decreasing horizontal hydraulic conductivity (equations (12) and (14)), with $\delta = 270$ m and $K_{sx} = 5.8 \times 10^{-6}$ m/s (solid curves) and constant hydraulic conductivity (equations (9) and (10)), with $K_x = 3.5 \times 10^{-7}$ m/s (dashed curves). The exponential K model allows for recharge velocities of $u_R \approx 0.5$ m/yr (large solid arrow) compared with $u_R \approx 0.1$ m/yr (small dotted arrow) for the constant K model (Figure 7a). As a result, the exponential K model shows larger horizontal flow vector components at shallower depths, reducing vertical flow velocities more rapidly with depth than the constant K model.

Therefore as expected, for a medium with exponentially decreasing hydraulic conductivity, the vertical groundwater flow velocity also decreases exponentially, from a recharge velocity of u_R at $z = 0$ with a skin depth (characteristic length scale) of δ.

[19] Figure 5 shows groundwater flow streamlines based on equations (9), (10), (12), and (14) for both constant and (in vertical direction) exponentially decreasing horizontal hydraulic conductivity. Input parameters for equations (9), (10), (12), and (14) are discussed in section 2.2.3 and Table 3. Figure 5 shows that the exponential K model causes streamlines to divert more rapidly into horizontal directions, allowing for a more rapid decrease in vertical groundwater flow velocity with depth than the constant K model.

[20] Substituting equation (14) into the steady state 1-D vertical heat advection-diffusion equation,

$$\gamma u_z \frac{\partial T}{\partial z} = D_m \frac{\partial^2 T}{\partial z^2}, \tag{15}$$

and integrating with respect to z and with boundary condition

$$\frac{\partial T}{\partial z}(z = b) = \left(\frac{\partial T}{\partial z}\right)_b \tag{16}$$

yields

$$\frac{\partial T}{\partial z} = \left(\frac{\partial T}{\partial z}\right)_b \exp\left[\frac{\gamma K_{sx}\delta}{D_m R}\left((b + \delta - z)e^{-b/\delta} - \delta e^{-z/\delta}\right)\right] \tag{17}$$

for exponentially decreasing hydraulic conductivity. Here, $(\partial T/\partial z)_b$ is the (conductive) background temperature gradient at the bottom of the aquifer and $\gamma = (\rho_w c_w)/(\rho_m c_m)$. To obtain $T(z)$, we integrate equation (17) numerically with respect to z and with boundary condition $T(z = 0) = T_R$, where T_R is the (near-surface) recharge temperature.

[21] In contrast to equation (17), for the case of constant hydraulic conductivity, i.e., linearly decreasing u_z, equation (10) is substituted into equation (15) and integrated twice with respect to z and with the same boundary conditions as for equation (17), resulting in

$$T = T_R - \left(\frac{\partial T}{\partial z}\right)_b \sqrt{\frac{\pi D_m R}{2\gamma \overline{K}_x}}\ \mathrm{erfc}\left[(b - z)\sqrt{\frac{\gamma \overline{K}_x}{2 D_m R}}\right]. \tag{18}$$

Here, erfc is the complementary error function. D_m in equations (15), (17), and (18), ρ_m, and c_m are mixed thermal

Table 3. Parameters for Coupled Groundwater and Heat Flow Models[a]

Symbol	Units	1-D$_c$	1-D$_e$	3-D Radial
$K_z(z)$	m/s	K_{sz}	$K_{sz}e^{-z/\delta}$	$\eta K_{sz}e^{-z/\delta}$
K_{sz}	m/s	3.5×10^{-7}	5.8×10^{-6}	3×10^{-8}
δ	m	∞	270	250
η		1	1	30
b	m	1000	1000	1200
h	m	x^2/R	x^2/R	TOPO
u_R	m/yr	0.1	0.5	1
T_r	°C	5	5	MALR
$(\partial T/\partial z)_b$	°C/m	0.042	0.040	0.067
H	W/m^2	0.84	0.080	0.134
ϵ	°C	0.68	0.92	$\sim$1

[a]The anisotropy ratio of horizontal to vertical hydraulic conductivity is given by $\eta = K_x/K_z$. For the radial model the recharge temperature is determined by the mean adiabatic lapse rate (MALR), and the upper hydraulic head, h, boundary is approximated by topography (TOPO). For the one-dimensional (1-D) models with constant hydraulic conductivity (1-D$_c$) and exponentially decreasing hydraulic conductivity (1-D$_e$), h is determined by the radius of curvature of the water table, $R = 10^5 \pm 2 \times 10^4$ m (Figure 4), and the horizontal distance, x, is determined from the maximum h in the recharge region.

diffusivity, mixed density, and mixed specific heat of the water-rock complex as defined in Appendix B.

[22] In section (2.2.3) we compare results for $T(z)$ from the exponential K (integral of equation (17)) and constant K (equation (18)) solutions and estimate groundwater recharge rates, u_R, characteristic depth scale, δ, aquifer thickness, b, and background heat flux,

$$H_b = -K_{T_r}\left(\frac{\partial T}{\partial z}\right)_b. \tag{19}$$

Here, K_{T_r} is the thermal conductivity of the rock alone, assumed to be on average about $K_{T_r} \approx 2\ \mathrm{Wm}^{-1}\mathrm{°C}^{-1}$, based on measurements on cores and cuttings from the Cascades [*Blackwell et al.*, 1982; *Ingebritsen et al.*, 1994].

2.2.2. Method: Radial Flow

[23] As described previously, owing to relatively low temperatures, we assume only gravity-driven advection and no density-driven flow. This allows us to first solve the steady state groundwater flow (hydraulic head diffusion) equation,

$$\frac{\partial}{\partial r}\left(K_r\frac{\partial h}{\partial r}\right) + \frac{K_r}{r}\frac{\partial h}{\partial r} + \frac{\partial}{\partial z}\left(K_z\frac{\partial h}{\partial z}\right) = 0, \tag{20}$$

for anisotropic and heterogeneous hydraulic conductivities, $\mathbf{K}_{rz}(rz)$, in a 3-D cylindrical coordinate system using only hydrogeologic and no thermal boundary conditions. Here, h is the variable hydraulic head and K_r and K_z are the hydraulic conductivities in the radial, r, and vertical, z, directions, respectively. This coordinate system is chosen because of the radial symmetry of Mount Hood (Figure 6), where the center of symmetry is approximated by the summit of the volcano. The outer vertical no flow boundary is chosen based on the occurrence of apparent groundwater-recharge-induced earthquakes (see section 2.3 as well as *Saar and Manga* [2003]) and on the existence of a borehole geotherm that shows a slight concave down temperature profile (triangles in Figure 8) suggesting upward flow of warmer water [*Bredehoeft and Papadopulos*, 1965]. The simulation domain has a radius of 7 km and a depth of 1.3 km.

[24] We solve equation (20) numerically by employing a finite difference algorithm with successively underrelaxed iterations [*Saar*, 2003]. The obtained hydraulic head field, $h(r, z)$, in the rz plane is then converted into a Darcy velocity field, $u(r, z)$, using a finite difference approach [*Saar*, 2003].

[25] We determine the temperature distribution by solving the steady state heat-advection-diffusion equation (without heat sources or sinks) in cylindrical coordinate form:

$$\frac{D_m}{\gamma}\left(\frac{\partial^2 T}{\partial r^2} + \frac{1}{r}\frac{\partial T}{\partial r} + \frac{\partial^2 T}{\partial z^2}\right) = -u_r\frac{\partial T}{\partial r} - u_z\frac{\partial T}{\partial z}, \tag{21}$$

where T, u_r, and u_z are temperature and Darcy velocities in the radial and vertical directions, respectively.

[26] Equation (21) is also solved using a finite difference approximation and successively underrelaxed iterations [*Saar*, 2003]. Boundary conditions for equations (20) and (21) are no groundwater and no heat flow boundary conditions, $\partial h/\partial r = 0$ and $\partial T/\partial r = 0$, at the central axis and at the outer vertical boundary. The lower boundary has mixed boundary conditions with no groundwater flow, $\partial h/\partial z = 0$, but constant heat flow boundary condition, $\partial T/\partial z = (\partial T/\partial z)_b$ = constant. Hydraulic head and temperature distribution along the upper boundary are a function of elevation, where the water table is assumed to be similar to the topography and temperature is approximated by the mean adiabatic lapse rate (MALR).

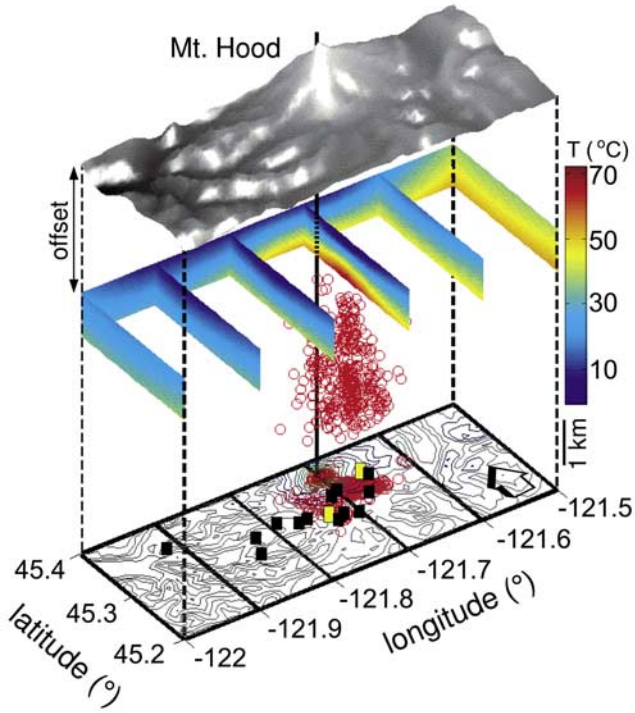

Figure 6. Shaded relief map of Mount Hood, Oregon (study region C in Figure 1), subsurface temperature distribution (color coded) based on a multiquadratic interpolation of 13 geotherms (black bars) and earthquake locations (red circles). The three geotherms closest to the summit of Mount Hood provide the measured $T(z)$ data in Figure 8. The relief map is vertically offset by 3 km (arrow) from the temperature map for better visualization of the temperature data. Elevated temperatures beneath Mount Hood appear to be offset toward the south (see vertical bar through the summit for comparison), consistent with the occurrence of the only two hot spring areas, Meadows Spring and Swim Warm Springs (yellow bars on elevation contour plot) observed, to date, at Mount Hood (Nathenson, submitted manuscript, 2003). Most earthquakes also occur beneath the southern flanks of the volcano (see projection of earthquakes onto map) and show mostly normal-fault focal mechanisms (see section 2.3, *Jones and Malone* [2002], and *Saar and Manga* [2003]).

[27] *Hurwitz et al.* [2003] suggest that water tables in volcanoes with ice caps may be much lower than the ground surface. However, for our approximate radial model the uncertainty associated with the unknown position of the water table is small compared with the overall model dimensions.

2.2.3. Results For 1-D and Radial Flow

[28] Figure 7a shows measured [*Blackwell*, 1992] and modeled temperature-depth profiles for the groundwater recharge region at Santiam Pass, Oregon. Solutions to both

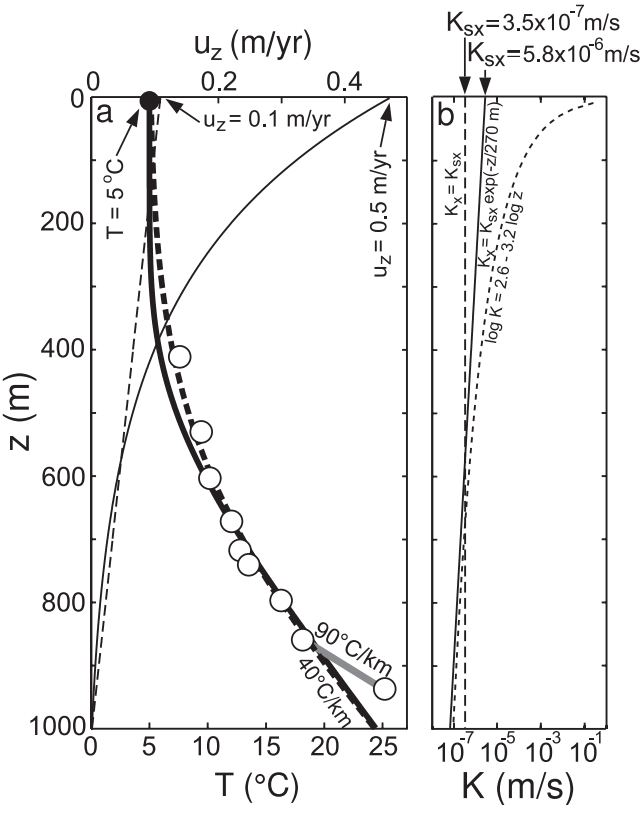

Figure 7. (a) Temperature-versus-depth models, $T(z)$ (bold curves), and vertical groundwater flow velocity profiles, $u_z(z)$ (thin curves), at Santiam Pass, Oregon. Dashed and solid curves indicate results based on constant and exponential horizontal hydraulic conductivity profiles, respectively (see Figure 7b). The $T(z)$ profiles are calculated from equation (18) and from numerical integration of equation (17) for constant and exponential hydraulic conductivity profiles, respectively. White-filled circles are temperature measurements from drill hole SP 77-24 [*Blackwell*, 1992] (for location, see Figures 1 and 4). The dark-filled circle is the mean annual surface temperature at nearby NOAA weather station 357559 (white arrow in Figure 4a) at Santiam Pass, Oregon, averaged over the last 10 available complete years (1975–1984) at an elevation of 1449 m. The precipitation rate at the same weather station is about 2.2 m/yr. The gray bold line connects the deepest two data points at a slope of about 90°C/km. The slope of the models at $z \approx 1000$ m is about 40°C/km. (b) Horizontal hydraulic conductivity, K_x, versus depth, z, for the constant $K_x = 3.5 \times 10^{-7}$ m/s model (long-dashed line) and the exponential $K_x = K_{sx} \exp(-z/\delta)$ model (solid line), with $K_{sx} = 5.8 \times 10^{-6}$ m/s and $\delta = 270$ m. The short-dashed curve is the permeability-depth curve suggested by *Manning and Ingebritsen* [1999] converted to z in m and hydraulic conductivity in m/s, assuming a constant temperature of about 20°C for estimates of water viscosity. Parameters are provided in Tables 1 and 3.

the constant (equation (18)) and the exponentially decreasing (integral of equation (17)) horizontal hydraulic conductivity model are provided. Both models suggest a very similar aquifer thickness, $b \approx 1000$ m, and background heat flux, $H_b \approx 0.080$ W/m^2 (Table 3). However, the constant K model requires a much lower recharge rate of $u_R \approx 0.1$ m/yr compared with the exponentially decreasing K model which allows for $u_R \approx 0.5$ m/yr. The larger recharge velocities in the latter case (thin solid curve in Figure 7a) are due to near-surface horizontal hydraulic conductivities of $K_{sx} = 5.8 \times 10^{-6}$ m/s that are about one order of magnitude larger than in the case of constant horizontal hydraulic conductivity where $K_x = 3.5 \times 10^{-7}$ m/s (Figure 7b). The mean absolute error between temperature data, T_D, and calculated temperatures, T_C, is given by $\epsilon = |T_D - T_C|/N$, where N is the number of measurements (including the surface temperature). The constant K model allows for a lower minimized error of $\epsilon \approx 0.68$°C compared with $\epsilon \approx 0.92$°C for the exponential K model. However, recharge rates of $u_R \approx 0.5$ m/yr, as suggested by the exponential model, are a more significant improvement because other studies [e.g., *Ingebritsen et al.*, 1994] suggest values of about $0.2 \leq u_R \leq 1$ m/yr. In addition, recharge rates of $u_R \approx 1$ m/yr are also supported by the results from our radial model discussed in the next paragraph.

[29] Figure 8 shows measured and calculated temperature-depth profiles for the three geothermal boreholes that fall within the radially symmetric model region at Mount Hood. Results agree well with the two deeper profiles but the shallow profile shows some deviations from measurements that are probably dominated by limitations in reducing the three dimensions into a 2-D cross section (i.e., owing to deviations from radial symmetry). Minimizing the misfit, ϵ, between model and data yields a horizontal near-surface hydraulic conductivity, $K_{xs} = 10^{-6}$ m/s, that is about 30 times larger than the vertical near-surface hydraulic conductivity, $K_{zs} = 3 \times 10^{-8}$ m/s. Both conductivities are assumed to decrease exponentially with depth according to a skin depth of $\delta = 250$ m. The simulation results also suggest a background heat flow of $H_b \approx 0.134$ W/m^2 and a recharge velocity of $u_R \approx 1$ m/yr (Table 3).

2.3. Groundwater-Recharge-Induced Seismicity Model: $k(z < 5$ km)

[30] *Saar and Manga* [2003] suggest that an increase in seismicity in late summer at Mount Hood, Oregon, is caused by seasonal groundwater recharge during spring due to snow melt on the flanks of the volcano. They show that a statistically significant correlation exists between groundwater recharge and seismicity. Groundwater recharge is approximated by discharge in runoff-dominated streams. The recharge in this region provides a natural pore fluid pressure signal of narrow temporal width and potentially relatively large amplitude. The pore fluid pressure pulse diffuses and can cause an effective stress decrease on preexisting faults at depth, effectively "unclamping" the fault and triggering earthquakes. *Saar and Manga* [2003] use the time lag between groundwater recharge and increased seismicity at a mean earthquake depth of 4.5 km to estimate (vertical) hydraulic diffusivity, D_z, for the depth range of $0 < z < 5 \times 10^3$ m, assumed to be homogeneous.

2.3.1. Method

[31] The solution to the one-dimensional (pressure) diffusion equation for periodic sinusoidal boundary conditions,

$$P'(t, z = 0) = P_0 \cos\left(\frac{2\pi t}{\psi}\right), \tag{22}$$

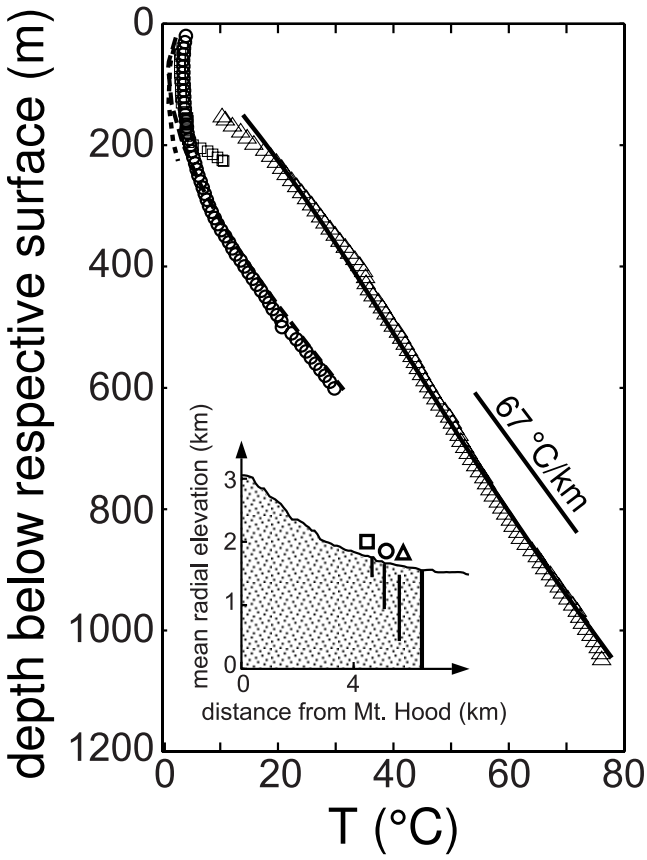

Figure 8. Temperature, T, versus depth, measured from the surface at each of the three geotherms at Mount Hood, Oregon, that are nearest to the summit (see the inset in this figure and black bars on the elevation contour plot in Figure 6). The solid, dashed, and dotted curves are results from the 3-D radial simulation. Measurements are indicated by triangles, circles, and squares. Two geotherms (circles and squares) show typical recharge-dominated profiles with an isothermal upper section, similar to the one shown in Figure 7a. The geotherm depicted by the triangles shows a mostly linear (conductive) profile with a slight concave-downward bend at shallower depths, suggesting a groundwater discharge region. Input parameters are discussed in the main text.

in a half-space is given by [*Turcotte and Schubert*, 2002]:

$$\frac{P'}{P_0} = \exp\left(-z\sqrt{\frac{\pi}{\psi D_z}}\right)\cos\left(\frac{2\pi t}{\psi} - z\sqrt{\frac{\pi}{\psi D_z}}\right), \qquad (23)$$

where P_0, P', ψ, t, and z are near-surface pore fluid pressure amplitude, pore fluid pressure amplitude at depth (in excess to hydrostatic pressure), period, time, and depth, respectively. The cosine term in equation (23) describes the phase lag of the pressure peak as a function of depth. *Saar and Manga* [2003] show that the argument in the cosine term is likely to be zero (or a multiple of 2π) and can thus be used to determine vertical hydraulic diffusivity:

$$D_z = \frac{\psi z^2}{4\pi t^2}. \qquad (24)$$

Equation (24) assumes pore fluid pressure diffusion in the saturated zone only and is thus sensitive to the location of the water table and the mean earthquake depth. As mentioned in section 2.2.2, *Hurwitz et al.* [2003] suggest that water tables in stratovolcanoes may be relatively deep. However, as described by *Saar and Manga* [2003] a low water table reduces both the diffusion depth, z, to earthquakes and the available diffusion time, t, in equation (24) cancelling the effects of each reduction. In addition, uncertainties in earthquake depths are large (±2 km) for the unrelocated earthquakes and are considered in the following section.

2.3.2. Results

[32] We use equation (24) to determine the large-scale vertical hydraulic diffusivity, D_z, for the upper 5 km of crust at Mount Hood, Oregon. The periodicity of groundwater recharge due to snow melt in spring is $\psi = 1$ year. The mean earthquake depth, $z = 4.5 \pm 2$ km, and time lag, $t = 151 \pm 7$ days (determined by cross correlations), provide the remaining parameters for equation (24), resulting in a hydraulic diffusivity of [*Saar and Manga*, 2003]

$$D_z = 0.30 \pm 0.22 \text{ m}^2/\text{s}. \qquad (25)$$

Hydraulic diffusivities of about 0.3 m^2/s for continental crust agree with values compiled by *Talwani and Acree* [1984] and are in the upper range for fractured igneous rocks [*Roeloffs*, 1996]. In fact, *Rothert et al.* [2003] report hydraulic diffusivities between 0.3 and 2 m^2/s for deeper (9.1 km), fractured crystalline crust at the German Continental Deep Drilling site (KTB) and diffusivities between 0.004 and 0.01 m^2/s for shallower (5.4 km), less fractured crust.

2.4. Magma Intrusion and Degassing Model: $k(z < 15$ km)

[33] The Cascades range is a volcanic arc located within the North American plate at its convergent boundary with the Juan de Fuca plate. Subduction zone related magmas intrude into the crust where they may (partially) solidify, assimilate crustal material, and/or erupt. Devolatilization of (mostly) water from solidifying magma provides a fluid source in the crust that, due to conservation of mass, is transmitted to the Earth's surface, unless consumed in metamorphic reactions. Owing to the large uncertainty range in magmatic volatile content considered in section 2.4.2, we neglect possible effects of metamorphic reactions on reducing the fluid flux. The volumetric fluid flux, Q, can be used to estimate vertical hydraulic conductivity, K_z, on a depth scale of about 15 km, i.e., from the estimated main magma intrusion depth to the surface (Figure 9). As before, within this region, K_z is assumed homogeneous.

2.4.1. Method

[34] The volumetric magma flux is given by

$$Q_M = q_M W, \qquad (26)$$

where q_M is the volumetric magma intrusion rate per kilometer arc length and W is the estimated arc width (Figure 9). We assume that only water devolatilizes. Therefore the volume flux of water, Q_w, released by the solidifying magma is given by

$$Q_w = \frac{q_M W \rho_M \phi_w}{\rho_w}, \qquad (27)$$

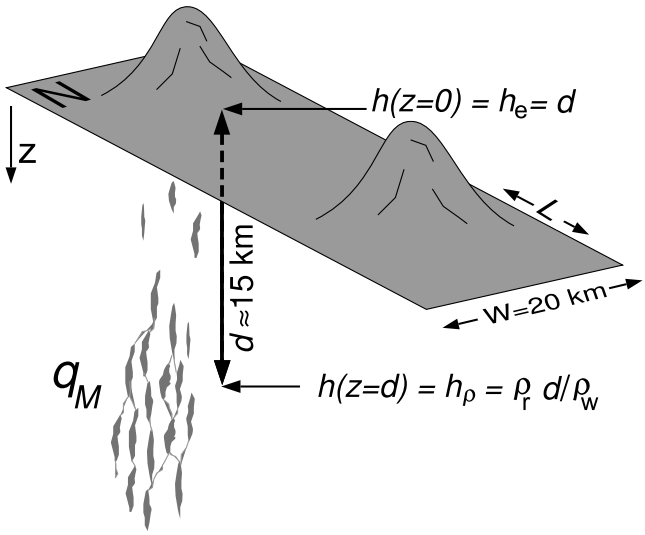

Figure 9. Schematic of magma intrusion underneath the Cascades range volcanic arc (not drawn to scale) [after *Hildreth*, 1981]. Symbols are defined in the main text.

where ϕ_w, ρ_M, and ρ_w are weight fraction of water content in the magma, and the densities of magma and water, respectively. In one (vertical) dimension, Darcy's law reduces to

$$|q_z| = \frac{Q_w}{A} = \left| -K_z \frac{\partial h}{\partial z} \right|, \tag{28}$$

where A and z are the total cross-sectional area perpendicular to the fluid flow direction and depth, respectively. Here, $A = WL$, where $L = 1$ km is the arc length considered for the volumetric magma intrusion rate, q_M, described previously. The hydraulic head, $h = h_e + h_p$, is the sum of elevation head, h_e, and pressure head, $h_p = P\rho_w^{-1}g^{-1}$, where P is the pore fluid pressure. At depth, z, the magma and its exsolved volatiles, such as water, are under lithostatic pressure so that $P = P_\ell \approx \rho_r g z$, where ρ_r is the mean rock density. At the surface ($z = 0$), P is given by the hydrostatic pressure, $P = P_h = \rho_w g z = 0$. Therefore if we set the arbitrary reference elevation to the magma intrusion depth, d, then $h(z = d) = h_p = \rho_r d/\rho_w$ and $h(z = 0) = h_e = d$. As a result, for any intrusion depth the hydraulic gradient is given by

$$\frac{\partial h}{\partial z} = \frac{h_p - h_e}{d} = \frac{\rho_r}{\rho_w} - 1. \tag{29}$$

Substituting equations (27) and (29) into equation (28) and recognizing that $A = WL$ yields the vertical hydraulic conductivity

$$K_z = \frac{Q_w}{A\left(\frac{\rho_r}{\rho_w} - 1\right)} = \frac{q_M \rho_M \phi_w}{L\ \rho_w \left(\frac{\rho_r}{\rho_w} - 1\right)}. \tag{30}$$

Applying $L = 1$ km, used for the volumetric magma intrusion rate per kilometer arc length, q_M, and rearranging yields

$$K_z = \frac{q_M \phi_w}{\left(\frac{\rho_r}{\rho_M} - \frac{\rho_w}{\rho_M}\right)}\ \ \mathrm{km}^{-1}. \tag{31}$$

Therefore K_z is independent of the assumed arc width, W. Assuming that, independent of subsurface temperature, $\rho_r \approx \rho_M$ reduces equation (31) to

$$K_z = \frac{q_M \phi_w}{\left(1 - \frac{\rho_w}{\rho_M}\right)} \mathrm{km}^{-1}. \tag{32}$$

Near the ground surface $\rho_w/\rho_M \approx 1/3$ and with increasing temperature at depth $\rho_w/\rho_M \to 0$ because ρ_w decreases and ρ_M remains relatively constant compared to ρ_w. Consequently, the term in the parentheses in equation (32) ranges between 2/3 and 1 for low and high temperatures, respectively, thus varying by a maximum factor of 1.5. In contrast, the much wider range of possible water fractions in the magma, $0.002 \le \phi_w \le 0.07$, allows for variations in K_z by a maximum factor of 35. Therefore we assume a constant water-magma density ratio of $\rho_w/\rho_M = 1/4$ for the elevated temperatures at depth, reducing equation (32) to

$$K_z = \frac{4}{3}\ q_M \phi_w\ \ \mathrm{km}^{-1}. \tag{33}$$

Equation (33) is independent of intrusion depth, d, because as depth increases, so does the lithostatic pressure, P_ℓ. However, d determines the depth scale for which K_z is determined. As before, within this depth scale, K_z is assumed homogeneous.

2.4.2. Results

[35] We use equation (33) to determine overall (assumed homogeneous) vertical hydraulic conductivity for the upper 15 km of the crust in the Cascades. As input data we assume a range of magma intrusion rates of $9 \le q_M \le 50$ km^3 Ma^{-1} km^{-1} [*Ingebritsen et al.*, 1989; *Blackwell et al.*, 1990]. *Sisson and Layne* [1993] and other authors [e.g., *Grove et al.*, 2002] suggest a magma water content of about 0.2 to over 3 wt % and up to 7 wt % for the Cascades arc including the Mount Shasta region in northern California. In addition, CO_2 may also be a significant volatile in subduction-related magmas, where carbonates may have been derived from subduction of marine sediments. To account for the uncertainty in volatile content, we apply a wide concentration range from 0.2 to 7 wt % (i.e., $0.002 \le \phi_w \le 0.07$) and assume it is all water. Substituting these values into equation (33) results in a range of vertical hydraulic conductivities of approximately

$$9 \times 10^{-13} \le K_z \le 2 \times 10^{-10}\ \mathrm{m/s} \tag{34}$$

for the deepest depth scale (15 km) considered.

3. Conversions Between *D*, *K*, and *k*

[36] In order to compare results from the four methods employed in this study we convert hydraulic diffusivity, D, and hydraulic conductivity, K, to permeability, k, assuming scalar quantities for the remainder of this paper. Transferring D to hydraulic conductivity,

$$K = DS_S, \tag{35}$$

requires assuming a value for specific storage:

$$S_S = \rho_w g(\alpha + n\beta), \tag{36}$$

Table 4. Conversions From Hydraulic Conductivity, K, to Permeability, k, and Parameters for Calculation of Respective Applicable Depth Ranges (z Ranges)[a]

		Column					
Symbol	Units	1	2	3	4	5	6
Method		spring discharge	heat flow	heat flow	heat flow	hydroseismicity	magma intrusion
Section		2.1	2.2	2.2	2.2	2.3	2.4
x, z		x	x	z	z	z	z
Study area		A	C1	B	C2	C3	D
EA, EH, PH		EA	EA	EH	EH	PH	PH
δ_{min}, δ_{max}	km	0.2, 0.3	0.2, 0.3	0.2, 0.3	0.2, 0.3	...	...
λ_{min}, λ_{max}		...	...	...	...	1, 10	1, 10
$b \pm 0.25b$	km	0.05 ± 0.0125	1 ± 0.25	1.2 ± 0.3	1.2 ± 0.3	4.5 ± 1.125	15 ± 3.75
z range	km	0.02–0.03	0.3–0.5	0.4–0.9	0.6–1.1	1.7–4.4	5.6–14.8
$(\partial T/\partial z)_b$	°C/km	50	50	50	50	50	50
z_m	km	0.025	0.4	0.65	0.85	3	10
T_m	°C	6	25	38	48	155	505
P_m	MPa	0.25	4	6.5	8.5	30	100
ρ_m	kg/m^3	10^3	10^3	10^3	10^3	10^3	0.5×10^3
μ_m	Pa · s	1.5×10^{-3}	8×10^{-4}	6×10^{-4}	5×10^{-4}	2×10^{-4}	5×10^{-5}
ν_m	m^2/s	1.5×10^{-6}	8×10^{-7}	6×10^{-7}	5×10^{-7}	2×10^{-7}	1×10^{-7}
K_{min}	m/s	10^{-3}	10^{-6}	3×10^{-7}	3×10^{-8}	8×10^{-8}	9×10^{-13}
K_{max}	m/s	10^{-2}	10^{-6}	3×10^{-6}	3×10^{-8}	5×10^{-7}	2×10^{-10}
k_{min}	m^2	1.5×10^{-10}	8.2×10^{-14}	1.8×10^{-14}	1.5×10^{-15}	1.6×10^{-15}	9×10^{-21}
k_{max}	m^2	1.5×10^{-9}	8.2×10^{-14}	1.8×10^{-13}	1.5×10^{-15}	1.0×10^{-14}	2×10^{-18}

[a]Conversions from hydraulic conductivity, K, to permeability, k, in horizontal, x, and vertical, z, directions based on equations (37) and (38). To calculate the mean kinematic viscosity, $\nu_m = \mu_m/\rho_m$ in equation (38), the mean temperature, $T_m = T_R + z_m (\partial T/\partial z)_b$, is determined where $T_R \approx 5$°C is a typical recharge temperature (Figures 7 and 8) and where $(\partial T/\partial z)_b \approx 50$°C/km (Figure 7 and section 4.2) in all cases. Here the applicable mean depth, z_m, is the average of the z range. The latter is calculated using combinations of minimum/maximum values for the aquifer depth, $b \pm 25\%$, and minimum/maximum skin depths, δ, or exponents, λ, for exponential, E, or power law, P, functions, respectively. The following refers to approximately horizontal layers without vertical fractures. The exponential solution, E, for the z range is used for shallower depths ($b \leq 2$ km), both for approximately horizontal (parallel) pathways (equation (49)) and for approximately vertical (serial) pathways (equation (46)) that are calculated using the arithmetic mean, A, and the harmonic mean, H, permeability expressions, respectively. The power law solution, P, is reserved for mean depths $z_m > 1$ km and is determined only for approximately vertical (serial) pathways (equation (47)) that are characterized by harmonic mean, H, permeability values. Resulting viscosities agree to within the implicit uncertainties with compilations by *Grigull et al.* [1990]. Hydraulic conductivity for column 5 (section 2.3) is based on results for vertical hydraulic diffusivity, D_z, and assuming $S_S \approx 10^{-6}$ m^{-1} in equation (35), as discussed in section 3. Permeability results are plotted in Figure 11b, where permeability uncertainties for columns 2 and 4 have been assigned ±1/2 order of magnitude based on the uncertainties calculated for k in columns 1, 3, 5, and 6.

where n is pore fraction, $\beta = 4.8 \times 10^{-10}$ m^2/N is the compressibility of water, and α is the bulk aquifer compressibility at constant vertical stress and zero lateral strain [*Wang*, 2000]. Further assumptions about temperature-dependent (and pressure-dependent) (dynamic) viscosity, μ, and water density, ρ_w, have to be made when converting hydraulic conductivity, K, to permeability, k, using

$$k = \frac{\nu K}{g}, \tag{37}$$

where the kinematic viscosity is given by $\nu = \mu/\rho_w$. Estimating α, ρ_w, and μ is not trivial and can lead to large uncertainties in inferred permeability values, particularly when converting from hydraulic diffusivity to permeability, where, in addition to ν, S_S has to be estimated. We assume $\alpha \approx 10^{-10}$ m^2/N for fractured igneous rock [*Roeloffs*, 1988; *Domenico and Schwartz*, 1998] and $n \approx 0.01$ [*Ingebritsen et al.*, 1992; *Hurwitz et al.*, 2003] yielding $S_s \approx 10^{-6}$ m^{-1}.

[37] Similar to *Germanovich et al.* [2000], we approximate kinematic viscosity as a function of depth-dependent mean temperature, T_m, for equation (37) by

$$\nu(T_m) \approx \frac{0.032 \text{ Pa} \cdot \text{s } ^\circ\text{C}}{\rho_w(1 - \alpha_w T_m)(15.4 \,^\circ\text{C} + T_m)}, \tag{38}$$

where $\alpha_w = 10^{-3}$°C^{-1} is the coefficient of thermal expansion of water and $\rho_w = 10^3$ kg/m^3 and $\rho_w = 0.5 \times 10^3$ kg/m^3 are the water densities for mean depths (and associated pressures and temperatures) $z_m \leq 3$ km and $z_m \approx 10$ km, respectively. For calculation of z_m and depth ranges (z ranges) over which our permeability results from the previous section are applicable, we refer to section 4 in conjunction with Table 4. The mean temperature is then given by $T_m \approx T_R + z_m (\partial T/\partial z)_b$ with a typical recharge temperature of $T_R \approx 5$°C (Figures 7a and 8) and a background temperature gradient of $(\partial T/\partial z)_b \approx 50$°C/km (Figures 7a and 8 as well as section 4.2). As we will show later, the depth ranges over which calculated permeabilities are applicable are independent of the actual permeability values. However, the z ranges do depend on the characteristics of the assumed decrease in permeability with depth (exponential versus power law relationship) and on the method for calculating the mean (arithmetic versus harmonic). Table 4 summarizes the hydraulic conductivities discussed in the previous section and the resulting permeabilities for the different depth scales.

4. Discussion

[38] In section 4.1 we discuss results from the previous two sections and suggest a curve describing permeability as a function of depth. In section 4.2 we address mean background heat flow values determined in section 2.2.

4.1. Heterogeneity and Anisotropy of Permeability

[39] Permeability, k, typically decreases with depth due to compaction, metamorphism, and/or filling of pore spaces

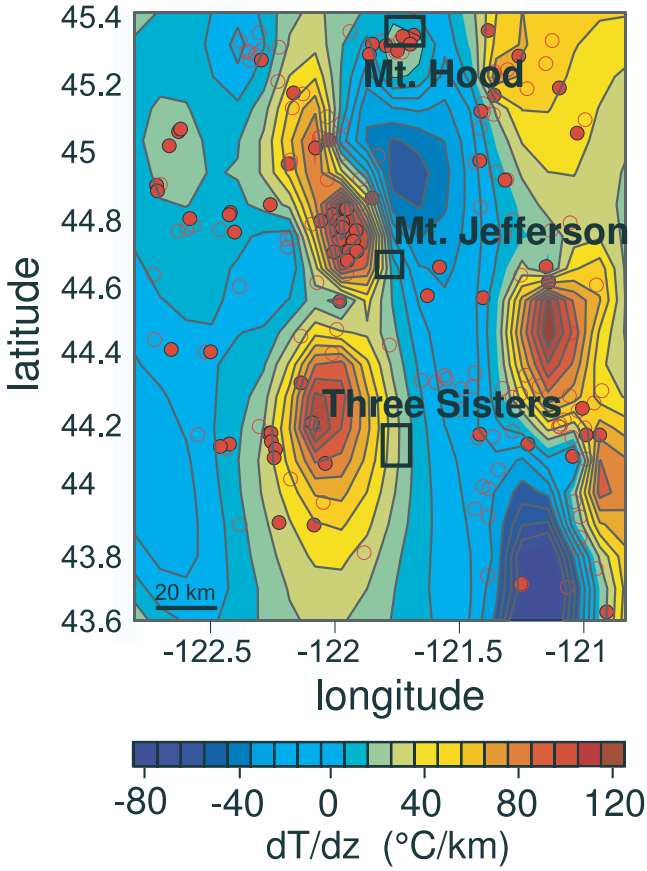

Figure 10. Map of near-surface temperature gradients in study region E (Figure 1) based on an interpolation of geotherm data from drill holes (circles). Isothermal and inverted temperature gradients exist in high-precipitation and groundwater recharge areas such as the high-relief volcanoes. Cold groundwater is heated at depth, and the heat is advected and discharged at hot springs [*Ingebritsen et al.*, 1989, 1992].

and fractures by precipitating minerals, particularly in hydrothermal regions [*Blackwell and Baker*, 1988; *Nicholson*, 1993; *Ingebritsen and Sanford*, 1998; *Fontaine et al.*, 2001]. In some cases, however, fractures can remain open due to earthquakes providing long-term (10s to 100s of years) high-k pathways [*Rojstaczer and Wolf*, 1992]. The characteristics of the reduction of k with depth, z, are difficult to determine and are controversial [e.g., *Gangi*, 1978; *Brace*, 1980, 1984; *Deming*, 1993; *Morrow et al.*, 1994; *Huenges et al.*, 1997; *Germanovich et al.*, 2001]. Several publications [e.g., *Belitz and Bredehoeft*, 1988; *Williams and Narasimhan*, 1989; *Manning and Ingebritsen*, 1999; *Shmonov et al.*, 2002; *Hurwitz et al.*, 2003; *Shmonov et al.*, 2003] as well as this study suggest a nonlinear decrease of k with z in the Cascades region and for continental crust in general. Nonlinear $k(z)$ profiles allow for high near-surface permeabilities and related high groundwater recharge rates so that the observed near-surface isothermal and inverted temperature-depth profiles are possible (Figures 7, 8, and 10). At the same time, a nonlinear $k(z)$ profile can reduce permeabilities to $k \leq 10^{-16}$ m^2 at $z \geq 4$ km, thus allowing for conduction-dominated heat transfer at these depths, as also required by observations [e.g., *Ingebritsen et al.*, 1992]. A transition from advection- to conduction-dominated heat transfer at $k \approx 10^{-16}$ m^2 has been suggested by numerous authors [*Norton and Knight*, 1977; *Smith and Chapman*, 1983; *Manning and Ingebritsen*, 1993; *Hayba and Ingebritsen*, 1997; *Huenges et al.*, 1997; *Manning and Ingebritsen*, 1999; *Clauser et al.*, 2002; *Hurwitz et al.*, 2003].

[40] In section 2.2, we invoked nonlinearity by decreasing permeability exponentially with depth. Figure 5 shows streamlines for constant (dashed curves) and exponentially decreasing (solid curves) k, where recharge rates for the latter are about 5 times larger than for constant k (thin lines near the surface in Figure 7a). The exponential $k(z)$ curve results in larger horizontal groundwater flow components at smaller depths, rapidly reducing vertical groundwater flow velocities and allowing for conduction-dominated heat transfer at relatively shallow depths.

[41] However, while exponential functions of (vertical) permeability, such as

$$k_z(z) = k_{zs} e^{-z/\delta}, \tag{39}$$

tend to provide reasonable near-surface (denoted with the subscript "s") values, including $k_z(z = 0) = k_{zs}$ at zero depth, they can also reduce permeability to unrealistically low magnitudes at depths greater than about 2 km (Figure 11b). In contrast, power laws, such as

$$k_z(z) = k_{zd}\left(\frac{z}{d}\right)^{-\lambda}, \tag{40}$$

provide larger, and thus more realistic, permeabilities at greater depths, but approach infinity for $z \rightarrow 0$ and result in a singularity for $z = 0$. They are thus defined for a finite depth, d, where $k_z(z = d) = k_{zd}$.

[42] Owing to these advantages and limitations of either function, we suggest equation (39) for $0 \leq z \leq 0.8$ km and equation (40) for $z > 0.8$ km. Equation (40) is equivalent to the curve suggested by *Manning and Ingebritsen* [1999] if $\lambda = 3.2$ and $k_{zd} = 10^{-14}$ m^2 at $d = 1$ km are chosen. In general, units of z and d have to be identical (e.g., both m or both km). Our results from section 2.2 suggest $\delta \approx 250$ m and $k_{zs} \approx 5 \times 10^{-13}$ m^2 for equation (39). For these values of λ, k_{zd}, δ, and k_{zs}, as well as for a depth of $z \approx 0.8$ km, the vertical permeabilities and their gradients,

$$-\frac{k_{zs}}{\delta} e^{-z/\delta} \approx -\frac{k_{zd}\lambda D^{\lambda}}{z^{\lambda+1}}, \tag{41}$$

are similar, thus enabling the suggested smooth transition from equation (39) to equation (40) at $z = 0.8$ km (Figure 11b).

[43] The methods employed and conversions discussed in sections 2 and 3 provide estimates of mean permeability at four depth scales, mostly in vertical, but in two cases also in approximately horizontal, directions. The spring discharge model (section 2.1) of study region A (Figure 1) yields an estimate of mean horizontal permeability, $\overline{k}_x$, because the method considers individual near-surface aquifers that consist of slope-parallel, and thus roughly horizontally layered, lava flows. Within such solidified lava flows (or aquifers),

water can flow primarily through the (about parallel and horizontal) pathways of highest permeability. Thus the mean horizontal permeability is given by the arithmetic mean [*Maasland*, 1957]

$$\overline{k}_x = \frac{1}{b}\sum_{i=1}^{N} k_{x_i} b_i, \tag{42}$$

where the subscript i denotes the ith layer or pathway, b_i is the thickness of layer i, and b is the total thickness of all layers.

[44] In contrast, vertical groundwater flow across horizontal lava flows (or aquifers) is passing through sections of varying permeability in series, so that mean vertical permeabilities are typically determined by the harmonic mean [*Maasland*, 1957]:

$$\overline{k}_z = b\left(\sum_{i=1}^{N} \frac{b_i}{k_{z_i}}\right)^{-1}, \tag{43}$$

where $\overline{k}_z$ is dominated by the lowest permeabilities along that path. Hence in volcanic or sedimentary settings, where slope-parallel, and thus approximately horizontal, layers, pathways, and aquifers are common, typically $10 \le \overline{k}_x/\overline{k}_z \le 1000$, at least near the surface [e.g., *Deming*, 1993] and in the absence of near-vertical fractures.

[45] A further consequence of $\overline{k}_z$ being determined by the harmonic mean (equation (43)) and $k_z(z)$ generally decreasing with depth is that our results for $\overline{k}_z$ from section 2 apply predominantly toward the lower portions of the considered depth ranges where the lowest permeabilities are encountered. Replacing the discrete layer formulation in equation (43) with the definite integral from zero to b of the continuous functions, equations (39) and (40), results in the harmonic mean vertical permeabilities

$$\overline{k}_z = \frac{b k_{zs}}{\delta(e^{b/\delta} - 1)} \tag{44}$$

and

$$\underline{k}_z = k_{zd}\left(\frac{D}{b}\right)^{\lambda}(\lambda + 1), \tag{45}$$

suggested for $0 \le z \le 0.8$ km and $z > 0.8$ km, respectively. Setting equation (39) equal to equation (44) and equation (40) equal to equation (45) provides the depths

$$\overline{z}_z = -\delta \ln\left[\frac{b}{\delta(e^{b/\delta} - 1)}\right] \tag{46}$$

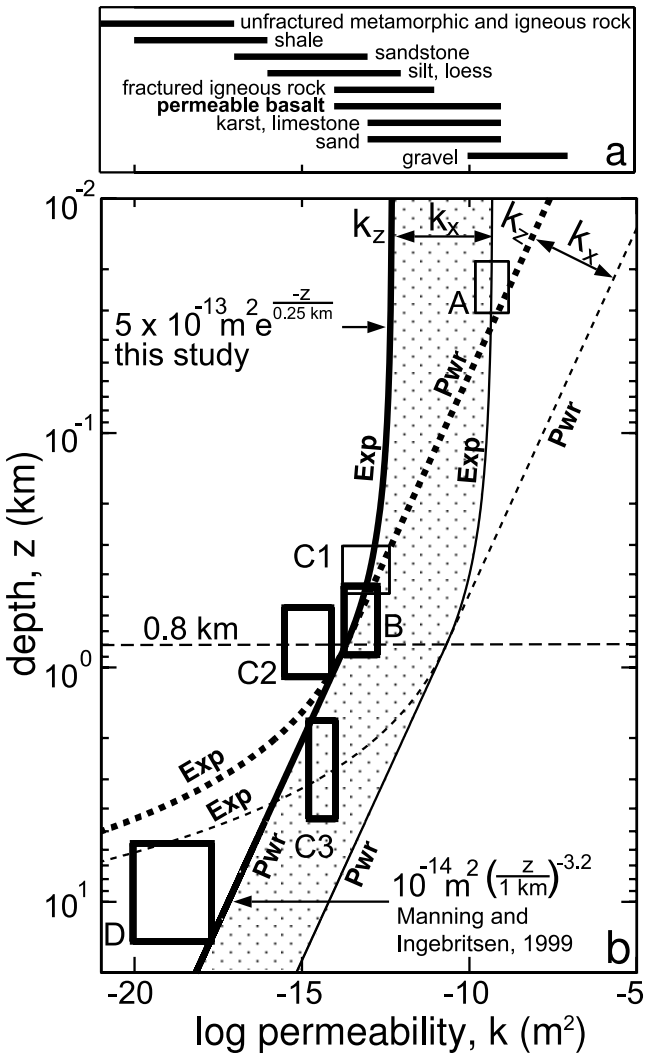

Figure 11. (a) Approximate (near-surface) range of permeability values [after *Freeze and Cherry*, 1979]. The (Oregon) Cascades primarily consist of basalt and basaltic andesite, where the youngest (<2.3 Ma) rock units of the High Cascades show high near-surface permeabilities of $k \approx 10^{-14}$ m^2 [*Ingebritsen et al.*, 1992, 1994], consistent with the k range indicated for permeable basalts. (b) Permeability, k, as a function of depth, z. Shown are our results for study regions A, B, C, and D (Figure 1 and Table 4) for horizontal, x (thin boxes), and vertical, z (bold boxes), permeabilities. The depth ranges are determined as described in the main text and in the caption to Table 4. Box widths and heights reflect approximate variations in permeability and applicable depth ranges, respectively, calculated from uncertainties in input parameters as described in section 4.1 and Table 4. Superimposed is the exponential profile of equation (39), denoted Exp, with δ = 0.25 km and $k_{zs} = 5 \times 10^{-13}$ m^2 for vertical (bold curve) and $k_{xs} = 5 \times 10^{-10}$ m^2 for horizontal (thin curve) permeabilities. Also shown is the power law profile of equation (40), denoted Pwr, with $\lambda = 3.2$ and $k_{zd} = 10^{-14}$ m^2 at d = 1 km, as suggested by *Manning and Ingebritsen* [1999] for vertical (bold line) permeabilities. $k_{zd} = 10^{-11}$ m^2 is used for horizontal (thin line) permeabilities. Solid lines indicate the permeability-depth curves suggested with a transition from exponential to power law profile at a depth of 0.8 km (dashed horizontal line). The dotted area indicates the expected range between vertical and horizontal permeability. At depth, this range may be expected to reduce due to compaction resulting in $k_x \rightarrow k_z$, which is not shown as the width of the dotted area remains constant. However, our results at $z \approx 0.5$ km suggest similar vertical (study region B) and horizontal (study region C1) permeabilities.

and

$$\underline{z}_z = b(\lambda + 1)^{-1/\lambda}, \quad (47)$$

where $\overline{k}_z$ and $\underline{k}_z$ are reached, respectively. Overbars and underbars in equations (44)–(47) and in later equations denote functions applicable to shallow (based on equation (39)) and deeper (based on equation (40)) depths, respectively. As before, b is the considered depth scale. Equations (46) and (47) are independent of the actual permeability value but depend on the characteristics of the decrease in permeability with depth (exponential versus power law relationship). We use equations (46) for depth scales, b, shallower than about 1 km and equation (47) for b greater than approximately 1 km. Parameter values of $200 \leq \delta \leq 300$ m, $1 \leq \lambda \leq 10$, and $b \pm 0.25b$ are based on results from section 2. These ranges in parameters are used to calculate the depth ranges (z ranges in Table 4 and Figure 11b) applicable to the shallower, $\overline{k}$, and deeper, $\underline{k}$, permeability results obtained in section 2.

[46] For the shallowest model (section 2.1 and study region A in Figure 1) the arithmetic mean horizontal permeability is determined. Here, each horizontal layer's permeability is assumed to decrease exponentially with depth according to equation (39). Similar to before, we replace the discrete formulation of the arithmetic mean (equation (42)) with the definite vertical integral from zero to b of the continuous function (equation (39)) resulting in the arithmetic mean horizontal permeability given by

$$\overline{k}_x = \frac{\delta k_{zs}}{b}\left(1 - e^{-b/\delta}\right). \quad (48)$$

Setting equation (39) and equation (48) equal yields the depth

$$\overline{z}_x = -\delta \ln\left[\frac{\delta}{b}\left(1 - e^{-b/\delta}\right)\right], \quad (49)$$

where $\overline{k}_x$ is reached. This depth, $\overline{z}_x$, is thus only based on the suggested ranges of maximum near-surface aquifer depths (thicknesses), $b = 50$ m $\pm$ 25%, and skin depths $200 \leq \delta \leq 300$ m (Table 4), where values for δ are inferred from our heat flow model (section 2.2). As before, the overbars in equations (48) and (49) denote functions applicable to shallower depths.

[47] Figure 11b shows our results for $\overline{k}_x$, $\overline{k}_z$, and $\underline{k}_z$ from section 2 at depths $\overline{z}_x$, $\overline{z}_z$, and $\underline{z}_z$ determined using equations (49), (46), and (47), respectively. This approach allows us to estimate depths, for which our permeability results are applicable, based on the shape of the $k(z)$ curve (exponential versus power law) and the method of calculating the mean (arithmetic versus harmonic) as also described in Table 4. Therefore while this technique does not use the actual (near-surface) permeability values, it requires assuming a model describing the change of permeability with depth (equations (39) and (40)). While the equations appear to describe $k_z(z)$ profiles in principle, the appropriate parameters are not well constrained and depend largely on the local geology. We thus use a wide range of values for δ, λ, and particularly b, as suggested previously, to calculate depth ranges (i.e., uncertainties) over which the mean permeabilities are applicable (Table 4).

[48] We recognize that our depth ranges are partially based on assuming that equation (40) applies for mean depths $z_m > 1$ km and are thus dependent on the curve suggested by *Manning and Ingebritsen* [1999], with $\lambda = 3.2$. However, we can use a wide range of $1 \leq \lambda \leq 10$ values to calculate a range of $\underline{z}_z$ using equation (47). For shallower mean depths of $0 \leq z_m \leq 1$ km and for vertical and horizontal permeabilities, we employ our suggested equations (46) and (49), respectively, that are instead based on equation (39). Here, we use $200 \leq \delta \leq 300$ m to determine ranges of $\overline{z}_z$ and $\overline{z}_x$. For either method we estimate independently a large uncertainty range in $b \pm 25\%$. Thus while $\underline{z}_z$ is not completely decoupled from $\lambda = 3.2$, the depth range is nonetheless based on an independent estimate of the maximum depth scale, b, a wide range of λ, and the reasonable assumption that the mean horizontal and vertical permeabilities are given by the arithmetic and the harmonic means, respectively, if approximately horizontal layers and no vertical fractures are present.

[49] Given the previous considerations, we suggest that our results for $k_z(z)$ and $k_x(z)$ in the Oregon Cascades are largely independent from, but comparable to, the permeability-depth profile suggested by *Manning and Ingebritsen* [1999] for the continental crust. However, we propose that for depths smaller than about 1 km, equation (39) with $k_{zs} \approx 5 \times 10^{-13}$ m^2 and $\delta \approx 250$ m is more appropriate at least for the Cascades and possibly for continental crust in general.

[50] For example, *Shmonov et al.* [2003] suggest a near-surface permeability of approximately $k_s \approx 2.75 \times 10^{-13\pm1.9}$ m^2 that decreases to $1.67 \times 10^{-20\pm1.5}$ at 40 km depth based on experimental data on the permeability of samples of amphibolite and gneiss from the Kola Ultradeep Borehole. Furthermore, D. Patriarche et al. (manuscript in preparation, 2004) invoke an exponential relationship between depth and hydraulic conductivity analogous to equation (39) with an average $\delta \approx 0.24$ km to satisfy calibrations for both measured hydraulic heads and ^{4}He concentrations in the sedimentary Carrizo aquifer in Texas. Because of the similarity of their δ value to ours ($\delta = 0.25$ km), their $K(z)$ curve (converted to $k(z) = K\nu/g \approx 10^{-7}K$) has a similar shape as our exponential $k(z)$ curve. Their zero-depth permeability of 5×10^{-11} m^2 is about two orders of magnitude larger than ours, is based on a near-surface hydraulic conductivity of the aquifer of about 5×10^{-4} m/s, and plots within the dotted region in Figure 11b.

[51] However, measurements from the German Continental Deep Drilling program (KTB) [*Huenges et al.*, 1997] show near-surface permeabilities of 5×10^{-18} to 3×10^{-16} m^2 that are much lower than those suggested by the $k(z)$ curve from *Manning and Ingebritsen* [1999] and significantly lower than even our suggested exponential $k(z)$ curve. Such low permeabilities may be expected in near-surface crystalline rocks at the KTB site. These rocks appear to show lower hydraulic diffusivities at shallower depths, probably due to higher fracture densities at greater depths, as reported by *Rothert et al.* [2003] and discussed briefly in section 2.3.2. *Huenges et al.* [1997] state that no clear depth dependence was observed. This, or even inverted $k(z)$ profiles, may be expected if near-surface permeabilities are so low that a reduction in permeability at depth, due to compaction of highly fractured sections, can be negligible.

[52] The range of measured (near-surface) permeability values, as well as the variance in depth dependence of permeability may serve as a reminder that a wide range of lithology-dependent permeabilities [e.g., *Freeze and Cherry*, 1979] is expected, particularly near the ground surface (Figure 11a). Our suggested exponential $k(z)$ curve falls within this wide range of permeabilities but of course cannot reflect all possible lithologies or degrees of fracturing. Instead, general $k(z)$ curves serve as permeability estimates at various depths over large spatial (and temporal) scales where more lithology-specific determinations are not feasible, as discussed further in sections 5 and 6. However, a maximum permeability value may be reached at about $k \approx 10^{-7}$ m^2 for gravel (Figure 11a). A more typical upper limit for continental crust in general may be $k \approx 10^{-12}$ m^2 [*Manning and Ingebritsen*, 1999, Table 1, Figure 8] at least in the vertical direction across horizontal layers. Such a low maximum average permeability further supports our exponential $k_z(z)$ relationship with the suggested finite near-surface value of about $k_{zs} \approx 5 \times 10^{-13}$ m^2 (Figure 11b) for vertical groundwater flow across subhorizontal lava flows or sedimentary layers and in the absence of near-vertical fractures.

[53] A further advantage of using equation (39) for depths shallower than about 1 km (or even shallower than 2 km) is that the function provides a finite near-surface permeability of k_{zs} as depth approaches zero. In contrast, equation (40) diverges toward infinity for $z \rightarrow 0$ and results in a singularity at $z = 0$. This limitation of equation (40) may not be critical for global studies of permeability, where overall estimates over larger depth scales ($z > 0.5$ km) may be desired. In fact, for $z > 2$ km, equation (40) is preferred because at greater depths its permeability gradient is smaller than the one for equation (39), providing more realistic deeper permeabilities. Therefore we propose a transition from equation (39) to equation (40) at $z = 0.8$ km. This transition is relatively smooth as permeabilities and their gradients (equation (41)) are comparable at $z = 0.8$ km (Figure 11b) for the suggested values of $k_{zs} \approx 5 \times 10^{-13}$ m^2, $\delta \approx 250$ m, $k_{zd} \approx 10^{-14}$ m^2, and $\lambda = 3.2$ (the latter two values are adopted from *Manning and Ingebritsen* [1999] and corroborated by this study). However, because of the similarity in permeabilities obtained from equations (39) and (40) for the suggested parameter values of k_{zs}, δ, k_{zd}, and λ and for $0.5 < z < 2$ km (Figure 11b) only equation (39) or only equation (40) may be used for $z < 2$ km and for $z > 0.5$ km, respectively. In contrast, if $k(z \geq 0$ km) is of interest, both equations should be employed with a transition at $z = 0.8$ km.

[54] However, if subvertical fractures and faults are present, high-k_z pathways can alter the relationship between depth and permeability. Hence we suggest that our elevated values of $k_z \approx 5 \times 10^{-15}$ m^2 at $z_m \approx 3$ km (Table 4 and Figure 11b), determined by the hydroseismicity method (section 2.3) for study region C3 (Figure 1), are due to faults located on the southern flanks of Mount Hood, such as the White River fault. These faults, that are located away from the volcano's central axis, show predominantly normal-fault focal mechanisms [*Jones and Malone*, 2002] and thus suggest tectonically driven (possibly hydrologically triggered [*Saar and Manga*, 2003]) earthquakes, rather than magma flow-induced seismicity that is typically characterized by nondouble-couple focal mechanisms [*Julian*, 1983; *Dreger et al.*, 2000]. Locally high values of k allow for advective heat transfer and hot springs, where water can reach the surface faster than heat diffusion timescales required for thermal equilibration with the surrounding rock. Indeed, the only two off-centered hot spring areas (Meadows Spring and Swim Warm Springs) observed at Mount Hood to date (M. Nathenson, Springs on and in the vicinity of Mount Hood, Oregon, submitted to *U.S. Geological Survey Open-File Report*, 2003, hereinafter referred to as Nathenson, submitted manuscript, 2003) are located on the southern flanks of the volcano close to the earthquakes' epicenters (Figure 6). Therefore we suggest that the slightly elevated permeabilities inferred for mean applicable depths of about $z_m = 3$ km in study region C3 (Figure 1 and Table 4) reflect the permeability of a large representative elementary volume that is dominated by normal faults that are being kept permeable by hydroseismicity [*Rojstaczer and Wolf*, 1992; *Townend and Zoback*, 2000]. In addition, vertical faults are approximately parallel to each other, thus providing parallel pathways whose combined mean permeability is dominated by the highest-k pathways which is determined by the larger arithmetic mean (equation (42)), rather than by the smaller harmonic mean (equation (43)) [*Rovey*, 1998].

[55] Scale dependence of permeability is controversial [*Brace*, 1980, 1984; *Clauser*, 1992; *Sánchez-Vila et al.*, 1996; *Renshaw*, 1998; *Rovey*, 1998; *Townend and Zoback*, 2000; *Zlotnik et al.*, 2000; *Hyun et al.*, 2002; *Becker and Davis*, 2003; *Zimmermann et al.*, 2003]. Permeability tends to increase as the representative elementary volume increases from laboratory rock-core measurements, over in situ field measurements, to large-scale regional models, as those considered in this study. This relationship may be the case because large-scale heterogeneities, that may include high permeability pathways, are more likely to be sampled if larger volumes are considered. For example this appears to be the case in the hydroseismicity model described in the previous paragraph. Therefore *Hsieh* [1998] suggests to call this sampling effect on inferred permeability values a "sampling bias" rather than a "scale effect." However, an upper bound appears to be reached at the upper field and regional modeling scale [*Clauser*, 1992; *Sánchez-Vila et al.*, 1996], possibly because most heterogeneities have been included [*Renshaw*, 1998].

4.2. Basal Heat Flow, H_b

[56] Figure 10 shows a map of vertical near-surface heat flow for study region E in Figure 1. The near-surface results are based on a multiquadratic interpolation technique [*Nielson*, 1993] applied to 209 geotherm boreholes and $K_{Tr} = 2$ W°C^{-1}m^{-1} [*Ingebritsen et al.*, 1988; *Blackwell*, 1992; *Ingebritsen et al.*, 1993]. High precipitation ($\sim$2 m/yr) and infiltration rates ($\sim$1 m/yr) in the Oregon Cascades cause isothermal (and sometimes inverted) near-surface geotherm profiles (Figures 7a, 8, and 10) effectively masking the background heat flow [*Ingebritsen et al.*, 1989, 1992]. We minimize the mean absolute error, ε, between data and calculated temperature values and infer a thermal gradient of about $(\partial T/\partial z)_b \approx 40$°C/km (Figure 7a) at Santiam Pass, located between two volcanoes, Three Fingered Jack and Mount Washington (Figure 4a). Connecting the deepest two

data points yields $(\partial T/\partial z)_b \approx 90°$C/km. However, the last data point was taken as drilling progressed [*Blackwell*, 1992]. Deeper portions of the linear temperature-depth profiles at Mount Hood volcano (Figure 8) yield $(\partial T/\partial z)_b \approx 65°$C/km. Therefore we infer a mean background heat flow, H_b, for the study region of approximately

$$0.080 \leq H_b \approx k_{T_R}\left(\frac{\partial T}{\partial z}\right)_b \leq 0.130 \text{ W/m}^2, \tag{50}$$

where the lower and upper heat flow values are inferred from the study of Santiam Pass and Mount Hood, respectively (Table 3). These values are consistent with the more extensive studies by *Blackwell et al.* [1982] and *Ingebritsen et al.* [1994]. As expected for a region showing active volcanism, heat flow is elevated with respect to global average values for continents of about 0.065 W/m^2 [*Pollack et al.*, 1993].

5. Implications

[57] As stated in the introduction, permeability largely determines subsurface fluid fluxes as well as energy transfer. Examples of subsurface fluids include water, steam, CO_2, noble gases, and hydrocarbons. Energy transfer may include pore fluid pressure diffusion and advective heat transport. In addition, transfer of heat and mass can cause fluid-rock interactions and metamorphic reactions. Therefore understanding spatial (and temporal) variations in permeability distributions has implications for studies involving groundwater, geothermal, ore, and hydrocarbon resources as well as for research addressing environmental contamination, carbon sequestration, and hydrologically induced earthquakes.

[58] Of particular interest for the Cascades investigated in this paper is the magnitude of advective heat transfer beneath the volcanoes which depends on the permeability distribution. This, in turn, has implications for background heat flow estimates, the shape and size of magmatic plumbing systems underneath subduction-related volcanoes, and the feasibility of geothermal energy exploration in the Oregon Cascades and geologically similar regions.

[59] Spatial (and temporal) scales of permeability distribution, and related mass and energy transfer patterns, can be highly variable as discussed in section 4.1. For small-scale, near-surface studies of fluid flow it is thus important to determine site-specific permeabilities employing for example permeameter or pumping tests. However, if the study region is large (hundreds to thousands of meters) model-based approximations of permeability as a function of depth as shown in Figure 11b may be a more representative description of the subsurface. In the latter case, the $k(z)$ relationship should be valid from shallow to large depths and should vary smoothly so that inferred models can be applied to all depths and abrupt refractions of flow lines are kept to a minimum. Both conditions are fulfilled for the composite $k(z)$ curve suggested in this study and summarized in equation (51).

6. Conclusions

[60] Because large-scale hydrogeologic models are generally underconstrained, it is desirable to utilize multiple direct and indirect observations to improve simulations, as described in the introduction. In this study, we use classic hydrogeologic boundary conditions and parameters as well as temperature and seismic data, and estimates of magma intrusion rates. Further improvements in future work may include additional constraints such as water chemistry and multiphase fluid flow, particularly at greater depths.

[61] We employ analytical and numerical modeling techniques to estimate permeability at different depth scales for the Oregon Cascades. Our results suggest that for depths shallower than about 1 km, permeability decreases exponentially with depth, with a skin depth of $\delta \approx 0.25$ km, from a near-surface value of $k_{zs} \approx 5 \times 10^{-13}$ m^2.

[62] For depths larger than about 1 km, permeability appears to decrease according to a power law as suggested by *Manning and Ingebritsen* [1999] with an exponent of $\lambda \approx 3.2$ and a permeability of $k_{zd} \approx 10^{-14}$ m^2 at depth $z =$ 1 km. Therefore we propose

$$k_z(z) = \begin{cases} 5 \times 10^{-13} \text{ m}^2 \ \exp\left(\dfrac{-z}{0.25 \text{ km}}\right) & \text{for } 0 \leq z \leq 0.8 \text{ km} \\ 10^{-14} \text{ m}^2 \ \left(\dfrac{z}{1 \text{ km}}\right)^{-3.2} & \text{for } z > 0.8 \text{ km}, \end{cases} \tag{51}$$

where the parameters for $z > 0.8$ km are adopted from *Manning and Ingebritsen* [1999] and are corroborated by this study. For studies that consider only depths <2 km or depths >0.5 km the respective exponential or power law functions can be employed without invoking a transition from one to the other at 0.8 km depth (see similarity between the functions at $0.5 < z < 2$ km in Figure 11b). However, if estimates of k_z are desired at all depths, the advantage of using both functions in equation (51) with a transition at $z = 0.8$ km is that they provide realistic average vertical permeabilities for both small ($z < 0.5$ km) and large ($z > 2$ km) depths which neither function alone could both achieve, as discussed in section 4.1. In addition, the functions in equation (51) yield a relatively smooth transition at $z = 0.8$ km, where their permeabilities and their permeability gradients are similar.

[63] We also determine horizontal permeabilities at depths shallower than about 1 km. At least near the surface, and in the absence of vertical fractures, horizontal permeabilities are typically one to three orders of magnitude larger in volcanic or sedimentary settings where slope-parallel, and thus approximately horizontal, layers, pathways, and aquifers are common.

[64] We note a slight divergence from equation (51) for our hydroseismicity model that suggests about one order of magnitude higher permeability values. However, higher permeabilities in this region may be consistent with advective heat transfer along active faults causing observed hot springs.

[65] Finally, our coupled heat and groundwater transfer models suggest groundwater recharge rates of $0.5 \leq u_R \leq$ 1 m/yr near the crest of the Cascades and mean background heat flow values of about $H_b \approx 0.080$ to $H_b \approx 0.134$ W/m^2 beneath the study region. The elevated background heat flow values are associated with volcanic centers that may have magma sources at shallower depths.

[66] Lithological variations and the degree of fracturing or dissolution can cause a wide range of permeabilities as

shown for example in Figure 11a. Therefore it is important to emphasize that the general relationship between depth and permeability suggested here (solid bold curve in Figure 11b and equation (51)) provides only a large-scale average estimate. This estimate was developed for the volcanic (Oregon) Cascades but may also apply to continental crust in general including sedimentary basins where near-horizontal layers are present. However, the suggested $k(z)$ relationship is not a substitute for more lithologically specific measurements of permeability for a given region of interest. However, frequently such direct permeability measurements are technically or economically not feasible at greater depths or over large regional scales. In such cases, estimates of the depth dependence of permeability, as presented here, can be useful.

Appendix A: Determination of the Recharge Velocity, u_R, For Exponentially Decreasing Hydraulic Conductivity in a 1-D Recharge Region

[67] In the xz plane (Figure 3), the recharge velocity, u_R, in equation (13) is given by the horizontal divergence (denoted $\nabla_x \cdot$) of the vertical integral over the depth of the saturated zone, b, of equation (7). For exponentially decreasing hydraulic conductivity, $K_x(z)$ in equation (7) is given by equation (11) resulting in

$$u_R = \nabla_x \cdot \left(-K_{sx} \nabla h(x) \int_0^b e^{-z/\delta} dz \right). \tag{A1}$$

Solving the definite integral in equation (A1) and expanding the divergence term yields

$$u_R = \nabla_x \left[-K_{sx}\delta \left(1 - e^{-b/\delta}\right) \right] \cdot \nabla_x h(x) - K_{sx}\delta \left(1 - e^{-b/\delta}\right) \nabla_x^2 h(x). \tag{A2}$$

At the maximum of the water table at $x = 0$, $\nabla_x h = 0$ and thus equation (A2) reduces to

$$u_R = \frac{K_{sx}\,\delta}{R} \left(1 - e^{-b/\delta}\right), \tag{A3}$$

where, as before, $R = -(\partial^2 h/\partial x^2)^{-1} = \nabla_x^2 h(x)$ is the (constant) radius of curvature of the water table in the xz plane.

Appendix B: Definition of Mixed Thermal Diffusivity, D_m

[68] For a given pore fraction, n, mixed properties, ξ_m, of the water-rock complex are approximated by

$$\xi_m = n\xi_w + (1 - n)\xi_r, \tag{B1}$$

where ξ_w and ξ_r are the properties in question of pure water and pure rock, respectively. Water-rock complex properties to be substituted into equation (B1), where subscripts remain as given in equation (B1), are mixed density, $\xi = \rho$, mixed specific heat, $\xi = c$, and mixed thermal conductivity, $\xi = K_T$. Mixed thermal diffusivity is then given by

$$D_m = \frac{K_{T_m}}{\rho_m c_m}. \tag{B2}$$

Throughout this analysis we assume local thermal equilibrium between water and rock and that n is sufficiently small so that equation (B1) applies.

[69] **Acknowledgments.** This work was supported by the Director, Office of Science, of the U.S. Department of Energy under Contract DE-AC03-76SF00098. We also thank the Sloan Foundation for support of this study and Steven Ingebritsen of the USGS at Menlo Park for making borehole temperature data available and for providing insightful comments on an earlier version of this manuscript. Chi-Yuen Wang is also thanked for providing feedback on the original manuscript. We are thankful to the U.S. Department of Commerce, National Oceanic and Atmospheric Administration (NOAA), for providing weather data on their Web site. Finally, we would like to extend special thanks to the two reviewers, John Costain and Shaul Hurwitz, as well as to associate editor Larry Mastin, whose insightful and detailed comments greatly benefited the final version of this manuscript.

References

Amit, H., V. Lyakhovsky, A. Katz, A. Starinsky, and A. Burg (2002), Interpretation of spring recession curves, *Ground Water*, *40*, 543–551.

Bear, J. (1988), *Dynamics of Fluids in Porous Media*, Dover, Mineola, N. Y.

Becker, K., and E. E. Davis (2003), New evidence for age variation and scale effects of permeabilities of young oceanic crust from borehole thermal and pressure measurements, *Earth Planet. Sci. Lett.*, *210*, 499–508.

Belitz, K., and J. D. Bredehoeft (1988), Hydrodynamics of the Denver Basin—Explanation of subnormal fluid pressures, *AAPG Bull.*, *72*, 1334–1359.

Blackwell, D. D. (1992), Thermal results of the Santiam Pass 77-24 drill hole, in *Geology and Geothermal Resources of the Santiam Pass Area of the Oregon Cascade Range, Deschutes, Jefferson, and Linn Counties, Oregon*, *Open File Rep. O-92-3*, edited by B. Hill, pp. 37–52, Oreg. Dep. of Geol. and Min. Ind., Portland.

Blackwell, D. D., and S. L. Baker (1988), Geology and geothermal resources of the Breitenbush-Austin hot springs area, Clackamas and Marion Counties, Oregon, in *Thermal Analysis of the Austin and Breitenbush Geothermal Systems, Western Cascades, Oregon*, *Open File Rep. O-88-5*, pp. 47–62, Oreg. Dep. of Geol. and Min. Ind., Portland.

Blackwell, D. D., R. G. Bowen, D. A. Hull, J. Riccio, and J. L. Steele (1982), Heat flow, arc volcanism, and subduction in northern Oregon, *J. Geophys. Res.*, *87*, 8735–8754.

Blackwell, D. D., J. L. Steele, S. Kelley, and M. A. Korosec (1990), Heat flow in the state of Washington and thermal conditions in the Cascade range, *J. Geophys. Res.*, *95*, 19,495–19,516.

Brace, W. F. (1980), Permeability of crystalline and argillaceous rocks, *Int. J. Rock. Mech. Min.*, *17*, 241–251.

Brace, W. F. (1984), Permeability of crystalline rocks: New in situ measurements, *J. Geophys. Res.*, *89*, 4327–4330.

Bredehoeft, J. D., and I. S. Papadopulos (1965), Rates of vertical groundwater movement estimated from the Earth's thermal profile, *Water Resour. Res.*, *1*, 325–328.

Clauser, C. (1992), Permeability of crystalline rocks, *Eos Trans. AGU*, *73*, 233–238.

Clauser, C., E. Griesshaber, and H. J. Neugebauer (2002), Decoupled thermal and mantle helium anomalies: Implications for the transport regime in continental rift zones, *J. Geophys. Res.*, *107*(B11), 2269, doi:10.1029/2001JB000675.

Deming, D. (1993), Regional permeability estimates from investigations of coupled heat and groundwater flow, North Slope of Alaska, *J. Geophys. Res.*, *98*, 16,271–16,286.

Domenico, P. A., and V. V. Palciauskas (1973), Theoretical analysis of forced convective heat transfer in regional ground-water flow, *Geol. Soc. Am. Bull*, *84*, 3803–3814.

Domenico, P. A., and F. W. Schwartz (1998), *Physical and Chemical Hydrogeology*, 2nd ed., John Wiley, Hoboken, N. J.

Dreger, D. S., H. Tkalcic, and M. Johnston (2000), Dilational processes accompanying earthquakes in the Long Valley caldera, *Science*, *288*, 122–125.

Fontaine, F. J., M. Rabinowicz, and J. Boulègue (2001), Permeability changes due to mineral diagenisis in fractured crust: Implications for hydrothermal circulation at mid-ocean ridges, *Earth Planet. Sci. Lett.*, *184*, 407–425.

Forster, C., and L. Smith (1989), The influence of groundwater flow on thermal regimes in mountainous terrain: A model and study, *J. Geophys. Res.*, *94*, 9439–9451.

Freeze, R. A., and J. A. Cherry (1979), *Groundwater*, Prentice-Hall, Old Tappan, N. J.
Gangi, A. F. (1978), Variation of whole and fractured porous rock permeability with confining pressure, *Int. J. Rock Mech. Min.*, *15*, 249–257.
Ge, S. (1998), Estimation of groundwater velocity in localized fracture zones from well temperature profiles, *J. Volcanol. Geotherm. Res.*, *84*, 93–101.
Germanovich, L. N., R. P. Lowell, and D. K. Astakhov (2000), Stress-dependent permeability and the formation of seafloor event plumes, *J. Geophys. Res.*, *105*, 8341–8354.
Germanovich, L. N., R. P. Lowell, and D. K. Astakhov (2001), Temperature-dependent permeability and bifurcations in hydrothermal flow, *J. Geophys. Res.*, *106*, 473–495.
Grigull, U., J. Straub, and P. Schiebener (1990), *Steam Tables in SI-Units*, 3rd ed., Springer-Verlag, New York.
Grove, T. L., S. W. Parman, S. A. Bowring, R. C. Price, and M. B. Baker (2002), The role of an H_2O-rich fluid component in the generation of primitive basaltic andesites and andesites from the Mt. Shasta region, N. California, *Contrib. Mineral. Petrol.*, *142*, 375–396.
Hall, F. R. (1968), Base-flow recessions: A review, *Water Resour. Res.*, *4*, 973–983.
Hayba, D. O., and S. E. Ingebritsen (1997), Multiphase groundwater flow near cooling plutons, *J. Geophys. Res.*, *102*, 12,235–12,252.
Hildreth, W. (1981), Gradients in silicic magma chambers: Implications for lithospheric magmatism, *J. Geophys. Res.*, *86*, 10,153–10,192.
Hsieh, P. A. (1998), Scale effects in fluid flow through fractured geologic media, in *Scale Dependence and Scale Invariance in Hydrology*, edited by G. Sposito, pp. 335–353, Cambridge Univ. Press, New York.
Huenges, E., J. Erzinger, J. Kück, B. Engeser, and W. Kessels (1997), The permeable crust: Geohydraulic properties down to 9101 m depth, *J. Geophys. Res.*, *102*, 18,255–18,265.
Hurwitz, S., S. E. Ingebritsen, and M. L. Sorey (2002), Episodic thermal perturbations associated with groundwater flow: An example from Kilauea Volcano, Hawaii, *J. Geophys. Res.*, *107*(B11), 2297, doi:10.1029/2001JB001654.
Hurwitz, S., K. L. Kipp, S. E. Ingebritsen, and M. E. Reid (2003), Groundwater flow, heat transport, and water table position within volcanic edifices: Implications for volcanic processes in the Cascade Range, *J. Geophys. Res.*, *108*(B12), 2557, doi:10.1029/2003JB002565.
Hyun, Y., S. P. Neuman, V. V. Vesselinov, W. A. Illman, D. M. Tartakovsky, and V. Di Federico (2002), Theoretical interpretation of a pronounced permeability scale effect in unsaturated fractured Tuff, *Water Resour. Res.*, *38*(6), 1092, doi:10.1029/2001WR000658.
Ingebritsen, S. E., and W. E. Sanford (1998), *Groundwater in Geologic Processes*, Cambridge Univ. Press, New York.
Ingebritsen, S. E., R. H. Mariner, D. E. Cassidy, L. D. Shepherd, T. S. Presser, M. K. Pringle, and L. D. White (1988), Heat-flow and water-chemistry data from the Cascade range and adjacent areas in north-central Oregon, *U.S. Geol. Surv. Open File Rep.*, *88-702*, 205 pp.
Ingebritsen, S. E., D. R. Sherrod, and R. H. Mariner (1989), Heat-flow and hydrothermal circulation in the Cascade range, north-central Oregon, *Science*, *243*, 1458–1462.
Ingebritsen, S. E., D. R. Sherrod, and R. H. Mariner (1992), Rates and patterns of groundwater flow in the Cascade range volcanic arc, and the effect of subsurface temperatures, *J. Geophys. Res.*, *97*, 4599–4627.
Ingebritsen, S. E., M. A. Scholl, and D. R. Sherrod (1993), Heat-flow from four new research drill holes in the western Cascades, Oregon, U.S.A., *Geothermics*, *22*, 151–163.
Ingebritsen, S. E., R. H. Mariner, and D. R. Sherrod (1994), Hydrothermal systems of the Cascades range, north-central Oregon, *U.S. Geol. Surv. Prof. Pap.*, *1044-L*, 86 pp.
James, E. W., M. Manga, T. P. Rose, and G. B. Hudson (2000), The use of temperature and the isotopes of O, H, C, and noble gases to determine the pattern and spatial extent of groundwater flow, *J. Hydrol.*, *237*, 100–112.
Jones, J. P., and S. Malone (2002), Mount Hood earthquake activity: Volcanic or tectonic origins?, *Eos. Trans. AGU*, *83*(47), Fall Meet. Suppl., Abstract S12A-1179.
Julian, B. R. (1983), Evidence for dyke intrusion earthquake mechanisms near Long-Valley caldera, California, *Nature*, *303*, 323–325.
Maasland, M. (1957), Drainage of agricultural lands, in *Soil Anisotropy and Soil Drainage*, edited by J. N. Maddock, pp. 216–285, Am. Soc. of Agron., Madison, Wis.
Manga, M. (1996), Hydrology of spring-dominated streams in the Oregon Cascades, *Water Resour. Res.*, *32*, 2435–2439.
Manga, M. (1997), A model for discharge in spring-dominated streams and implications for the transmissivity and recharge of Quaternary volcanics in the Oregon Cascades, *Water Resour. Res.*, *33*, 1813–1822.
Manga, M. (1999), On the timescales characterizing groundwater discharge at springs, *J. Hydrol.*, *219*, 56–69.
Manga, M. (2001), Using springs to study groundwater flow and active geologic processes, *Annu. Rev. Earth Planet. Sci.*, *29*, 201–228.
Manning, C. E., and S. E. Ingebritsen (1993), Missing mineral zones in contact metamorphosed basalts, *Am. J. Sci.*, *293*, 894–938.
Manning, C. E., and S. E. Ingebritsen (1999), Permeability of the continental crust: Implications of geothermal data and metamorphic systems, *Rev. Geophys.*, *37*, 127–150.
Meinzer, O. E. (1927), Large springs in the United States, *U.S. Geol. Surv. Water Supply Pap.*, *557*, 94 pp.
Morrow, C., D. Lockner, S. Hickman, M. Rusanov, and T. Rockel (1994), Effects of lithology and depth on the permeability of core samples from the Kola and KTB drill holes, *J. Geophys. Res.*, *99*, 7263–7274.
Nicholson, K. (1993), *Geothermal Fluids: Chemistry and Exploration Techniques*, Springer-Verlag, New York.
Nielson, G. M. (1993), Scattered data modeling, *IEEE Comput. Graphics*, *13*, 60–70.
Norton, D., and J. E. Knight (1977), Transport phenomena in hydrothermal systems: Cooling plutons, *Am. J. Sci.*, *277*, 937–981.
Phillips, O. M. (1991), *Flow and Reactions in Permeable Rocks*, Cambridge Univ. Press, New York.
Pollack, H. N., S. J. Hurter, and J. R. Johnson (1993), Heat flow from the Earth's interior: Analysis of the global data set, *Rev. Geophys.*, *31*, 267–280.
Renshaw, C. E. (1998), Sample bias and the scaling of hydraulic conductivity in fractured rock, *Geophys. Res. Lett.*, *25*, 121–124.
Roeloffs, E. A. (1988), Fault stability changes induced beneath a reservoir with cyclic variations in water level, *J. Geophys. Res.*, *93*, 2107–2124.
Roeloffs, E. A. (1996), Poroelastic techniques in the study of earthquake-related hydrologic phenomena, *Adv. Geophys.*, *37*, 135–195.
Rojstaczer, S., and S. Wolf (1992), Permeability changes associated with large earthquakes—An example from Loma-Prieta, California, *Geology*, *20*, 211–214.
Rothert, E., S. A. Shapiro, S. Buske, and M. Bohnhoff (2003), Mutual relationship between microseismicity and seismic reflectivity: Case study at the German Continental Deep Drilling Site (KTB), *Geophys. Res. Lett.*, *30*(17), 1893, doi:10.1029/2003GL017848.
Rovey, C. W. (1998), Digital simulation of the scale effect in hydraulic conductivity, *Hydrogeol. J.*, *6*, 216–225.
Saar, M. O. (2003), Geological fluid mechanics models at various scales, Ph.D. thesis, Univ. of Calif., Berkeley.
Saar, M. O., and M. Manga (1999), Permeability-porosity relationship in vesicular basalts, *Geophys. Res. Lett.*, *26*, 111–114.
Saar, M. O., and M. Manga (2003), Seismicity induced by seasonal groundwater recharge at Mt. Hood, Oregon, *Earth Planet. Sci. Lett.*, *214*, 605–618.
Sánchez-Vila, X., J. Carrera, and J. P. Girardi (1996), Scale effects in transmissivity, *J. Hydrol.*, *183*, 1–22.
Shmonov, V. M., V. M. Vitovtova, A. V. Zharikov, and A. A. Grafchikov (2002), Fluid permeability of the continental crust: Estimation from experimental data, *Geochem. Int.*, *40*, suppl. 1, 3–13.
Shmonov, V. M., V. M. Vitiovtova, A. V. Zharikov, and A. A. Grafchikov (2003), Permeability of the continental crust: Implications of experimental data, *J. Geochem. Explor.*, *78–79*, 697–699.
Singh, K. P., and J. B. Stall (1971), Derivation of base flow recession curves and parameters, *Water Resour. Res.*, *7*, 292–303.
Sisson, T. W., and G. D. Layne (1993), H_2O in basalt and basaltic andesite glass inclusions from 4 subduction-related volcanoes, *Earth Planet. Sci. Lett.*, *117*, 619–635.
Smith, L., and D. S. Chapman (1983), On the thermal effects of groundwater flow: 1. Regional scale systems, *J. Geophys. Res.*, *88*, 593–608.
Sorey, M. L. (1971), Measurement of vertical groundwater velocity from temperature profiles in wells, *Water Resour. Res.*, *7*, 963–970.
Tallaksen, L. M. (1995), A review of baseflow recession analysis, *J. Hydrol.*, *165*, 349–370.
Talwani, P., and S. Acree (1984), Pore pressure diffusion and the mechanism of reservoir-induced seismicity, *Pure Appl. Phys.*, *122*, 947–965.
Townend, J., and M. D. Zoback (2000), How faulting keeps the crust strong, *Geology*, *28*, 399–402.
Turcotte, D. L., and G. Schubert (2002), *Geodynamics*, 2nd ed., Cambridge Univ. Press, New York.
Wang, H. F. (2000), *Theory of Linear Poroelasticity*, Princeton Univ. Press, Princeton, N. J.

Williams, C. F., and T. N. Narasimhan (1989), Hydrogeologic constraints on heat-flow along the San-Andreas fault—A testing of hypotheses, *Earth Planet. Sci. Lett.*, *92*, 131–143.

Woodbury, A. D., and L. Smith (1988), Simultaneous inversion of hydrogeologic and thermal data: 2. Incorporation of thermal data, *Water Resour. Res.*, *24*, 356–372.

Woodbury, A. D., L. Smith, and W. S. Dunbar (1987), Simultaneous inversion of hydrogeologic and thermal data: 1. Theory and application using hydraulic head data, *Water Resour. Res.*, *23*, 1586–1606.

Zimmermann, G., H. Burkhardt, and L. Engelhard (2003), Scale dependence of hydraulic and structural parameters in the crystalline rock of the KTB, *Pure Appl. Geophys.*, *160*, 1067–1085.

Zlotnik, V. A., B. R. Zurbuchen, T. Ptak, and G. Teutsch (2000), Support volume and scale effect in hydraulic conductivity: Experimental aspects, *Spec. Pap. Geol. Soc. Am.*, *348*, 215–231.

M. Manga, Department of Earth and Planetary Science, University of California, 173 McCone Hall, Berkeley, CA 94720-4767, USA. (manga@eps.berkeley.edu)

M. O. Saar, Department of Geological Sciences, University of Michigan, 2534 C.C. Little Building, 425 East University Avenue, Ann Arbor, MI 48109-1063, USA. (msaar@umich.edu)